Geothermics 138 (2026) 103638

Contents lists available at ScienceDirect

Geothermics

journal homepage: www.elsevier.com/locate/geothermics

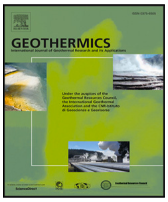

Electrical thermal response test

Clarissa Szabo-Som [a],*, Gabriel Fabien-Ouellet [a], Philippe Pasquier [a], Adrien Dimech [b]

[a] Polytechnique Montréal, P.O. Box 6079, Station Centre-Ville, Montréal, H3C 3A7, QC, Canada
[b] École de technologie supérieure, 1100 Rue Notre Dame Ouest, Montréal, H3C 1K3, QC, Canada

ARTICLE INFO

Dataset link: https://github.com/GeoCode-polymtl/E-TRT

Keywords:
Thermal response test
Electrical resistivity monitoring
Thermal parameter estimation
Volumetric heat capacity

ABSTRACT

Thermal response tests (TRT) are commonly used to estimate the ground thermal conductivity k and, to a lesser extent, the volumetric heat capacity C_s. While k can be estimated with relatively good accuracy, the estimation of C_s is typically less accurate, mainly because this volumetric property is inferred from point temperature measurements collected only within the borehole. The present work addresses this limitation by introducing an electrical TRT (E-TRT) that performs electrical resistivity (ER) monitoring during a conventional TRT. To analyse the experimental measurements, a coupled thermal–electrical model was developed to simulate the ER response to temperature variations during heat injection in a standing column well. Bayesian inversion was applied to both direct temperature and ER datasets. A synthetic experiment confirms that ER data are sensitive to C_s as well as the ER temperature coupling parameter m, and reduces uncertainty of C_s by about 50% to 70%. A field validation during a 256-hour E-TRT resulted in stable estimates of all parameters, with uncertainties of 3.8% for k, 12.4% for C_s and 4.7% for m. E-TRT offers an approach that can help estimate C_s and provide a field-scale alternative to laboratory-based measurements in estimating m. This strategy can be extended to monitor the entire standing column well and adapted to closed-loop systems.

1. Introduction

Low-temperature geothermal systems are used for both heating and cooling buildings and rely on ground heat exchangers (GHE) to transfer thermal energy between the subsurface and a heat pump. GHEs can take various forms, typically involving the circulation of a heat carrier fluid through a closed-loop piping network (Lund and Toth, 2021) or through open-walled boreholes that utilize groundwater directly (Rees et al., 2004). The design of a GHE requires knowledge of the local thermal properties, more specifically the thermal conductivity k and the volumetric heat capacity C_s. The thermal conductivity is considered the most critical parameter influencing GHE performance after advective heat transfer (Wagner and Clauser, 2005). However, under dynamic heat loads, the volumetric heat capacity affects heat dissipation and introduces a delay in the temperature response relative to the applied heat flux (Huang et al., 2020). Furthermore, the thermal diffusivity, defined as the ratio $\alpha = k/C_s$, describes a material's ability to conduct thermal energy relative to its capacity to store it (Márquez et al., 2016). This parameter influences the long-term temperature response of the GHE, as the spatial extent of heat transfer expands over time (Li et al., 2019).

The thermal properties are typically estimated at a given site using a thermal response test (TRT) (Gehlin, 2002), which involves circulating a heated fluid through the GHE and recording temperature variations at the borehole inlet and outlet over time. The interpretation of conventional TRTs is usually based on the first-order approximation of the infinite line source model (Ingersoll, 1954), in which the volumetric heat capacity C_s is assumed known. Since C_s cannot be estimated using this approach (Raymond et al., 2011), more accurate numerical models can be used to improve thermal parameter estimations. Finite element methods, for instance, allow for a detailed representation of the GHE, incorporating elements such as pipe geometry, fluid properties, and temporal variations in the heat injection rate (Signorelli et al., 2007; Özüdoğru et al., 2014). These models can also account for geological heterogeneities and fractures, including advective heat transfer processes (Signorelli et al., 2007; Robert et al., 2022; Beaudry et al., 2018). Such models are typically coupled with optimization algorithms to minimize the least-squares error between simulated and measured temperature responses (Spitler and Gehlin, 2015). Nevertheless, the relatively low sensitivity of borehole temperature measurements to C_s (Pasquier, 2015; Wagner and Clauser, 2005) leads to poor resolution, and C_s is often kept fixed during optimization (Pasquier et al., 2019).

Due to this low sensitivity, a high uncertainty is typically associated with C_s (Wagner and Clauser, 2005; Raymond et al., 2011; Li et al., 2019). The few attempts to estimate it have relied on Bayesian inference approaches coupled with the use of surrogate models to reduce

---

* Corresponding author.
E-mail address: clarissa.szabo-som@etud.polymtl.ca (C. Szabo-Som).

https://doi.org/10.1016/j.geothermics.2026.103638
Received 16 December 2025; Received in revised form 10 February 2026; Accepted 13 February 2026

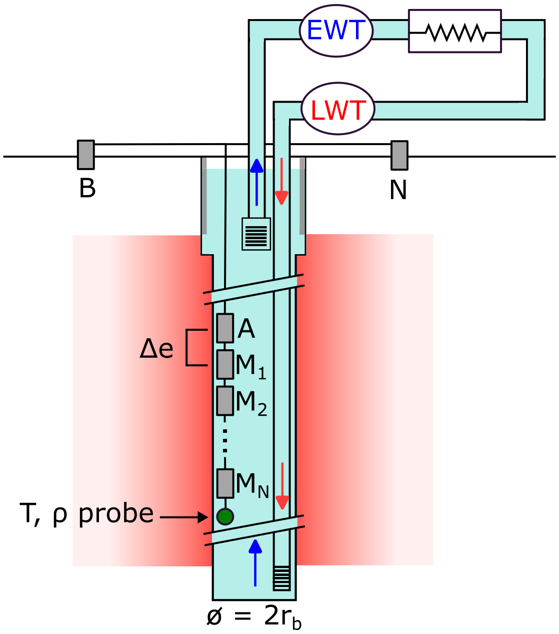

Fig. 1. Conceptual presentation of the electrical survey of a thermal response test (E-TRT) on a standing column well (SCW). The red represents temperature conduction in the bedrock around the SCW.

computational burden. For instance, Pasquier and Marcotte (2020) used a neural network and the temporal correlation of the residuals to estimate the joint distribution of five parameters, including the volumetric heat capacity, with an uncertainty of 16.3% for a 168-hour TRT performed on a closed-loop GHE. Jacques and Pasquier (2023) applied the same approach to experimental data collected on a standing column well and obtained an estimated uncertainty of 14% for the volumetric heat capacity. Despite those efforts, the reliable determination of the volumetric heat capacity remains challenging (Pasquier and Marcotte, 2020), mainly due to the physical location of the temperature measurements, which are, at best, taken along a line within the borehole and not directly within the geological material itself.

Geophysical methods can provide complementary measurements to those obtained in GHEs. Indeed, they are designed by nature to image the spatial distribution of subsurface properties, offering a valuable complement to point-based direct temperature measurements. Electrical resistivity, in particular, is sensitive to temperature variations (Revil et al., 1998) and can serve as a proxy to track heat propagation in the bedrock during a TRT. Several authors have used electrical resistivity tomography (ERT) in different contexts to image the spatio-temporal dynamics of thermal plumes (Hermans et al., 2012; Arato et al., 2015; Giordano et al., 2017; Comina et al., 2019; Kyrkou et al., 2024). These applications are relatively recent and have expanded significantly in recent years (Dimech et al., 2022). Surface measurements have also been used to visualize temperature variations induced by a closed-loop GHE energy storage system (Comina et al., 2019; Giordano et al., 2017; Arato et al., 2015) or by the injection of heated water in a screened well at low depths (Hermans et al., 2012; Lesparre et al., 2019). Shariatinik et al. (2024) used cross-borehole ERT during a heat tracer experiment to recover the variability of hydrological parameters. In a heat tracer experiment, Hermans et al. (2015) compared temperatures derived from cross-hole ERT with direct measurements, and reported errors of 10%–20%. Such large discrepancies are expected for surface or cross-hole ERT, since the resulting images depend strongly on the type of regularization used to solve the inverse problem, often limiting their quantitative use for parameter estimation. Furthermore, the typical resolution of surface or cross-hole ERT is insufficient to image the thermal disruption occurring in a TRT, which rarely reaches beyond 2 m of the borehole wall.

Similar to ERT, electrical logging probes are designed for continuous electrical resistivity measurements along a single borehole. The simplest probe configurations are the short and long-normal, with a geometry of two electrodes inside the borehole spaced 16 and 64 inches apart, respectively, connected to two surface electrodes (Doll, 1953). As a tool for quantitative interpretation, the difference in sensitivity of the electrode spacing in the borehole can be leveraged to invert for the resistivity of different zones in the rock formation (Itskovich et al., 1998; Goswami et al., 2004; Ulugergerli, 2011; Tsourlos et al., 2003). Typical electrical logging is sensitive to electrical variations near the borehole wall, where temperature disturbances are expected during a TRT.

To improve thermal parameter estimation during a TRT, we propose complementing temperature measurements with borehole electrical resistivity (ER) measurements. By injecting current and recording voltages using electrodes placed in a borehole as illustrated in Fig. 1, electrical resistivity variations within the surrounding rock formations can be quantified. Owing to the linear relationship between electrical conductivity and temperature (Hayley et al., 2007), ER measurements provide information on the propagation of thermal disturbances in the rock, offering additional constraints on thermal parameter estimation.

The present work describes a novel procedure, which we refer to as an electrical thermal response test (E-TRT). Through numerical and field experiments, we demonstrate that monitoring the electrical response with borehole electrodes during a TRT allows for better constraints on thermal parameter estimation, particularly the volumetric heat capacity. The paper first outlines the general E-TRT methodology, including data acquisition and processing. Synthetic experiments are then presented to validate this new procedure and to confirm and quantify improvements in thermal parameter estimation over standard TRT. Finally, the applicability of the method is demonstrated with a field application on a standing column well (SCW) at a well-documented experimental site located in the city of Varennes, Canada, shown in Fig. 2.

2. Methodology

The E-TRT we propose consists of using ER measurements to monitor temperature variations around the GHE during the TRT. Fig. 1 displays a general acquisition setup. The E-TRT contains two parts: a standard TRT and an ER monitoring survey conducted simultaneously.

2.1. Conventional thermal response test

The standard TRT follows a defined protocol, beginning with the recirculation phase, which serves to homogenize water temperature distribution inside the GHE. The initial temperature T_0 is measured either along the borehole using a temperature probe or using distributed temperature sensing (DTS) (Spitler and Gehlin, 2015). Then, the heating phase involves heating the circulating water at a constant heating power q and measuring temperature variation through time at the borehole inlet (LWT) and outlet (EWT), as shown in Fig. 1. Finally, the recovery phase consists of ceasing heat injection and maintaining recirculation, while still measuring temperature variations.

2.2. Electrical thermal response test

For the ER monitoring survey, a multi-electrode cable, such as the one illustrated in Fig. 2(c) is placed in the borehole before starting the TRT and kept at a fixed position throughout the duration of the E-TRT, to maintain spatial consistency and avoid field issues, such as disruption of the heat injection process or cable entanglement. Such a multi-electrode cable can be used in uncased boreholes or within screened PVC casings. As shown in Fig. 2(a), the cable is connected

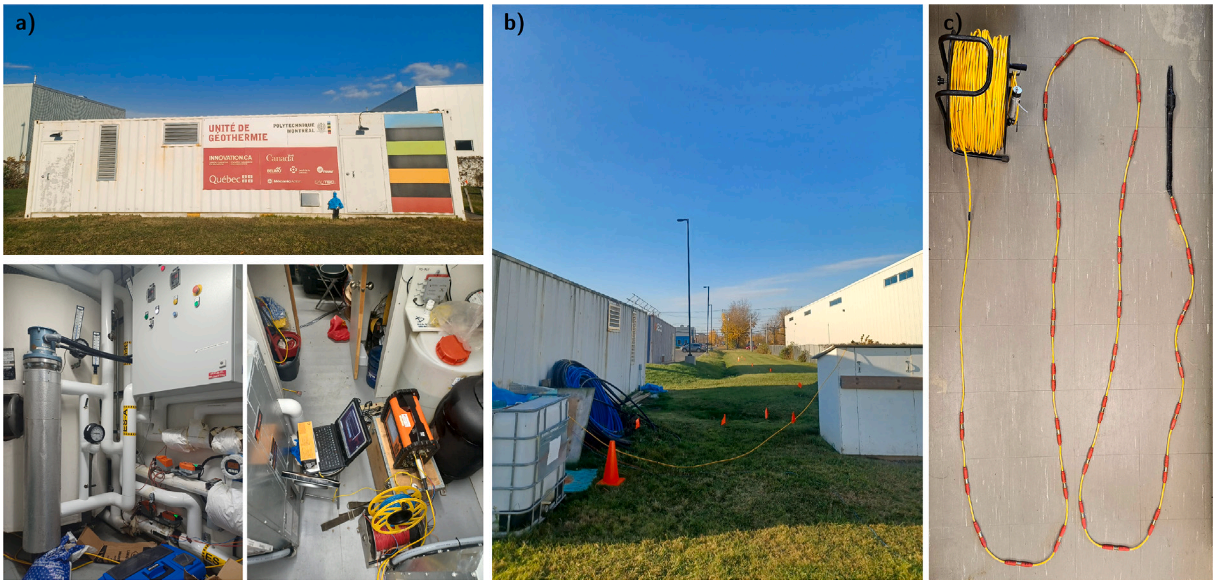

Fig. 2. Field photographs illustrating the experimental setup at the Varennes site: (a) Exterior (top) and interior (bottom) views of the Mobile Geothermal Laboratory, which houses the control systems for the thermal response test and the geoelectrical instrumentation used for continuous monitoring, (b) View of the SCW with the geoelectrical cable exiting the wellhead and routed into the laboratory, (c) Close-up of the geoelectrical cable installed inside the SCW, featuring 32 electrodes spaced at 25 cm intervals.

to a resistivity meter that can inject current and read voltages at any combination of the connected electrodes. Repeated ER surveys are carried out at various time intervals during the heating phase, starting at the end of the recirculation phase, which acts as a reference. The geometry of the electrodes and cable, the measuring protocol employed and the temporal resolution of the sampling all influence the sensitivity of the measurements.

Relevant parameters are the electrode spacing Δe and the number of electrode pairs N_e, as they impact the spatial resolution, the radial depth of investigation, and the length of the borehole that is monitored. Since the thermal modelling assumes radial conductive heat transfer, the cable should be installed at a depth where the rock formation is thermally homogeneous and exempt from fractures.

In this study, we use a pole–pole electrode configuration as shown in Fig. 1 in which the reference electrodes (current return B and potential reference N) are placed at the surface and assumed to be at infinity, and two active electrodes (current A and potential M) are placed inside the borehole. The distance between A and M is varied by measuring at different electrode positions along the cable. Because only the current electrode A is located inside the borehole, this configuration reduces sensitivity to current channelling in the borehole water, which generally exhibits higher electrical conductivity than the surrounding bedrock. To approximate ideal boundary conditions, surface electrodes are placed at a distance of at least 20 times the separation between active electrodes. This configuration is preferred for small spacings, as larger spacings can increase telluric noise (Loke, 2001).

The measurement protocol defines the sequence of electrode positions that are used for measurements during each acquisition time step. The temporal resolution is determined by both the duration of each acquisition cycle and the frequency at which these protocols are executed (Dimech et al., 2022). A comprehensive strategy involves measuring the potential across all electrodes for every injection electrode, maximizing spatial coverage. However, for long electrode arrays, this exhaustive approach can become time-intensive and may result in information loss if the resistivity of the rock formation varies more rapidly.

The resulting ER measurements consist of voltages ΔV and currents I, which are transformed into apparent resistivity ρ_a by:

$$\rho_a = \frac{\Delta V}{I} K, \tag{1}$$

where K is a geometric factor that depends on the electrode locations. The apparent resistivity represents an effective resistivity for a homogeneous medium (Binley and Slater, 2020), and provides an averaged measurement over a volume proportional to the electrode spacing.

2.3. Thermal–electrical modelling and inversion

Estimating thermal parameters from an E-TRT requires modelling both the thermal and electrical responses within the GHE and the surrounding rock mass. These modelled responses are then compared with field data, and thermal parameters are inferred through error minimization. The overall workflow is shown in Fig. 3, and its main components are described below.

2.3.1. Thermal response model

Conventional TRT interpretation relies on the measured temperature data to recover the thermal parameters of the ground and the GHE. Inverse methods are employed to minimize the error between measured and modelled values of the average borehole fluid temperature $\overline{T}_f$ at time t due to a heating power q and relatively to an initial temperature T_0. Heating power q is measured during the TRT and directly governs heat propagation in the bedrock and fluctuations in q affect the accuracy of conventional TRT data (Florides and Kalogirou, 2008). This approach integrates the equivalent thermal conductivity k_{eq}, volumetric heat capacity C_{eq}, and the borehole's thermal resistance R_b, according to:

$$\overline{T}_f(t) = T_0 + q(t)R_b + \Delta T\left(r_b, t; k_{eq}, C_{eq}, q\right). \tag{2}$$

This study focuses on SCWs, as shown in Fig. 1, which are a type of open-walled GHE, where groundwater fills the borehole and is directly used as the heat carrier fluid. For SCWs, fluid temperature is near the borehole wall temperature, meaning that R_b is near 0 (Spitler et al., 2002; Jacques et al., 2025). As this work focuses on SCWs, we omit R_b in what follows. However, note that an E-TRT should be applicable to most types of GHEs, and R_b could be included among the estimated parameters, if required.

The temperature variation at the borehole wall, $\Delta T(r_b, t) = \overline{T}_f - T_0$, is evaluated using the infinite cylindrical source (ICS) model (Carslaw and Jaeger, 1959). This choice strikes a balance between improved accuracy

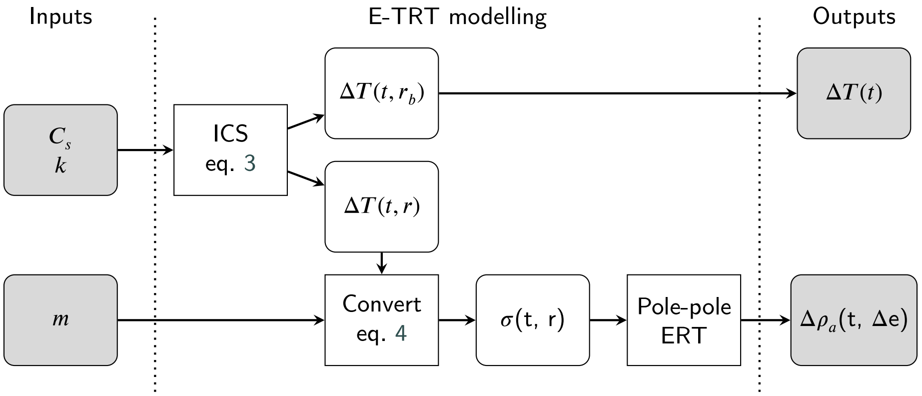

Fig. 3. Summarized description of the forward model of the electrical survey on a thermal response test.

on the geometry of SCWs compared to the infinite line source (Ingersoll, 1954) and the high computational cost of numerical models. However, there are no limitations to employing more advanced modelling for E-TRT when needed.

For the ICS model, heat is emitted from an infinitely long cylinder of radius r_b with an initial constant temperature. The resulting spatiotemporal temperature variation within the rock formation is given by:

$$\Delta T(r,t) = \frac{q}{k\pi^2}\int_0^\infty \left(e^{-\beta^2 z} - 1\right) \frac{J_0(p\beta)Y_1(\beta) - Y_0(p\beta)J_1(\beta)}{\beta^2\left(J_1^2(\beta) + Y_1^2(\beta)\right)}\, d\beta, \tag{3}$$

where $z = \alpha t/r_b^2$, $p = r/r_b$, where J_0 and J_1 are Bessel functions of the first type and of the zero and first order, and where Y_0 and Y_1 are Bessel functions of the second type. Such models are deemed accurate for long-term estimation of the borehole response, after a characteristic time ($t_b = 5r_b^2/\alpha$).

2.3.2. Electrical resistivity relationship with temperature

To simulate the ER response during an E-TRT, the temperature–resistivity relationship has to be defined. For geological materials exempt from metallic minerals, the bulk electrical conductivity is the sum of two contributions: conduction through the electrolytic pore fluid and surface conduction along mineral surfaces, particularly in clay-rich materials (Archie, 1942; Waxman and Smits, 1968). Both are sensitive to temperature variations (Revil et al., 1998; Hayley et al., 2007). At low temperatures and for small temperature variations, the relationship between bulk electrical conductivity and temperature is linear and given by:

$$\sigma_T - \sigma_0 = \sigma_0 m \Delta T, \tag{4}$$

where σ_T is the electrical conductivity at temperature T, and σ_0 is the electrical conductivity at reference temperature T_0. The term ΔT denotes the temperature difference ($\Delta T = T - T_0$) and m represents the fractional change in conductivity per degree Celsius (Hayley et al., 2007). This formulation assumes either a proportional contribution of surface and electrolyte conductivity or negligible surface conduction (Hayley et al., 2007). For near-surface applications, within the temperature range of 3 to 40 °C, the ratio model is preferred over other temperature correction approaches (Ma et al., 2011). Surface conduction is negligible in clean sand where the value of m ranges from 0.018 to 0.025 $°\mathrm{C}^{-1}$, and is often determined through laboratory calibration using site-specific water samples (Hermans et al., 2012; Giordano et al., 2017; Comina et al., 2019). In high-temperature geothermal environments, studies on clay-altered rocks have shown that this linear relationship holds between 25 to 50 °C and up to approximately 150 °C (Nono et al., 2020; Kristinsdóttir et al., 2010). Nono et al. (2020) report m values ranging from 0.021 to 0.0925 for altered volcanic rocks, while Kristinsdóttir et al. (2010) estimate values between 0.036 and 0.28 for smectite and chlorite altered rocks at temperatures between 40 and 100 °C. The variability of m for geological materials suggests that it should be estimated on a site-specific basis. In what follows, m will be estimated based on the joint measurements of temperature and electrical resistivity.

2.3.3. Electrical resistivity modelling

The electrical response of an E-TRT is simulated with the SimPEG Python library (Cockett et al., 2015; Heagy et al., 2017). The governing equation for DC resistivity is from Maxwell's equation for the electric potential V and can be described in the form of a Poisson equation:

$$\nabla \cdot \left(\frac{1}{\rho(\boldsymbol{x})}\nabla V(\boldsymbol{x})\right) = -I\delta\left(\boldsymbol{x}_c\right) \tag{5}$$

where ρ is the electrical resistivity, I is the injected current at the location of the current electrode $\boldsymbol{x}_c$, and $\delta(\cdot)$ is the Dirac delta function (Binley and Slater, 2020). This equation is solved numerically using a finite volume method on a cylindrical mesh using the `discretize` and `mesh` modules (Heagy et al., 2017). The mesh increases logarithmically at the top and bottom of the cylinder and radially, where we use Dirichlet boundary conditions of null potential. The numerical method is chosen because no analytical solution exists for the time-varying electrical resistivity distribution encountered in an E-TRT. For the E-TRT, the strong effect of the borehole water resistivity on the ER measurement necessitates a 3D model (Nimmer et al., 2008) with an explicit representation of the borehole (Doetsch et al., 2010) in the forward simulation to help reduce borehole-related artifacts. Consequently, the electric model comprises a large axisymmetric cylindrical grid, minimizing boundary effects, subdivided into two regions: (1) the SCW, located centrally with a radius r_b, and (2) the surrounding bedrock formation. The simulation follows a radial model, centred on the axis of the SCW, under the assumption of vertical homogeneity. Electrical resistivity measurements are simulated for a pole–pole survey with electrodes A and M at $r = 0$ and reference electrodes B and N at infinity. With the assumption that the electrodes are far from the surface, we can consider a whole space. The geometry of the electrodes replicates the experimental setup illustrated in Fig. 1.

2.3.4. Joint thermal–electrical model

Joint electrical–thermal modelling begins with the definition of a reference model. At the end of the recirculation phase, we assume that the temperature within the SCW and the surrounding bedrock has reached thermal equilibrium, such that both share the same initial temperature T_0. We also assume a homogeneous bedrock conductivity σ_0, which is reasonable given the short electrode array and its limited radial sensitivity (< 2 m). The value of σ_0 is estimated through a least-squares fit of the reference ER data, using the fixed, measured groundwater conductivity inside the SWC $\sigma_{w,0}$. In practice, vertical variations in bedrock conductivity may occur due to lithologic changes

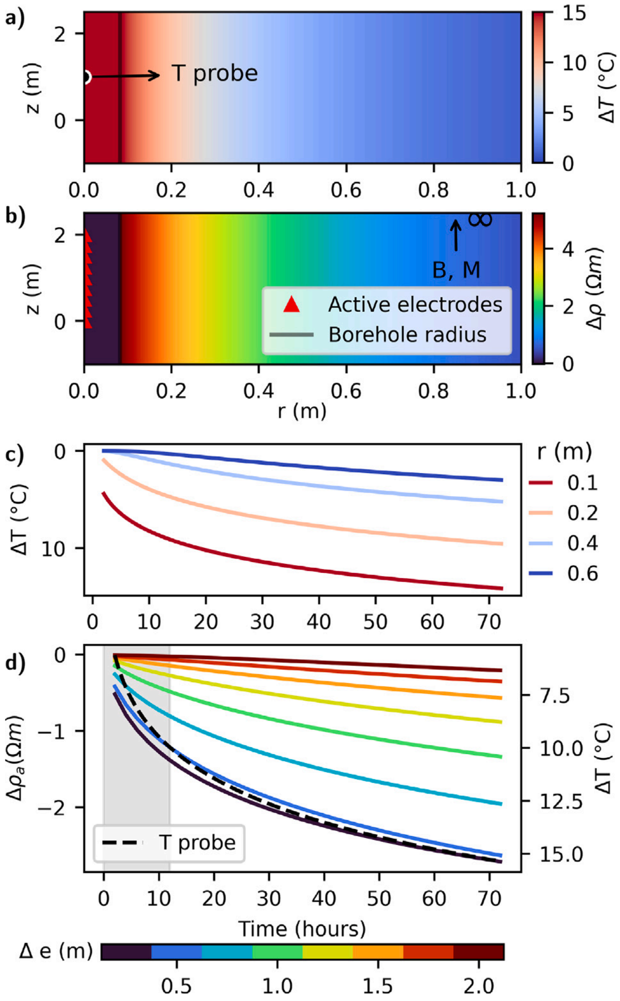

Fig. 4. Spatial axisymmetric model of the synthetic E-TRT after 72 h of heating. (a) Temperature distribution simulated by the ICS, with the model's vertical extent shown along the z-axis. (a) Corresponding 2D variation in electrical resistivity. Active electrodes are positioned at the centre of the grid, while surface electrodes are assumed to be located at an infinite distance at the top boundary. (c) Temporal temperature variation in the bedrock at different radial distances. (d) Resulting synthetic apparent resistivity and temperature temporal data.

or the presence of fractures. Drilling disturbances may also introduce radial conductivity variations. Under such conditions, a spatially varying reference conductivity $\sigma_0(z,r)$ can be recovered using a standard regularized inversion.

The thermal and ER measurements are simulated for different time steps after the start of heating at a constant heat flux q (W/m). Temperature variations at the borehole wall $\Delta T(t, r_b)$ and in the surrounding bedrock $\Delta T(t,r)$ are simulated with the ICS (Eq. (3)) which are then converted to electrical conductivity $\sigma(t,r)$ with Eq. (4). Figs. 4(a) and 4(b) illustrate an example of the temperature variations around the borehole under the infinite axial grid, and its transformation into resistivity. Note that the electrical conductivity inside the borehole is obtained from direct measurements of the water. Given $\sigma(t,r)$, the pole–pole electrical resistivity survey is simulated for all time-steps by solving Eq. (5). The apparent resistivity is computed with Eq. (1) and apparent resistivity variations are obtained by subtracting the reference value $\Delta\rho_a(t,\Delta e) = \rho_a(t,\Delta e) - \rho_a(0,\Delta e)$. Note that measurement times for temperature and ER measurements usually differ. Using variations in resistivity rather than absolute values further mitigates any undesirable borehole effects (Nimmer et al., 2008; Doetsch et al., 2010), while highlighting the model's ability to replicate dynamic resistivity responses.

This procedure simulates the full E–TRT dataset $\mathbf{d} = [\mathbf{\Delta T}^\top \; \mathbf{\Delta \rho_a}^\top]^\top$, which is composed of two parts:

1. **Temperature variations $\mathbf{\Delta T}$** measured at the cable depth, where $\Delta T_i = \Delta T(t_{T,i})$ and $t_{T,i}$ denotes the N_T discrete temperature measurement times.
2. **Apparent resistivity variations $\mathbf{\Delta \rho_a}$**, where $\Delta\rho_{a,ij} = \Delta\rho_a(t_{\rho,i}, \Delta e_j)$. Here, $t_{\rho,i}$ represents the N_ρ discrete resistivity measurement times, and Δe_j denotes the N_e electrode spacings.

2.3.5. *Parameter estimation*

We use Bayesian inference to estimate the electro-thermal parameters, regrouped in the vector $\mathbf{m} = [k \; C_s \; m]^\top$. We seek to estimate the posterior probability distribution $p(\mathbf{m}|\mathbf{d})$, given a prior distribution of the model parameters $p(\mathbf{m})$ and the likelihood $p(\mathbf{d}|\mathbf{m})$ which describes the probability of observing the data $\mathbf{d}$ obtained given a certain model $\mathbf{m}$ (Tarantola, 2005):

$$p(\mathbf{m}|\mathbf{d}) \propto p(\mathbf{d}|\mathbf{m})p(\mathbf{m}). \tag{6}$$

Assuming multivariate normally distributed random variables for both measurements and model parameters, we can write the prior as

$$p(\mathbf{m}) \propto \exp\left[-\frac{1}{2}(\mathbf{m}-\mathbf{m}_{\text{prior}})^\top \mathbf{C}_{\text{m}}^{-1}(\mathbf{m}-\mathbf{m}_{\text{prior}})\right], \tag{7}$$

and the likelihood as

$$p(\mathbf{d} \mid \mathbf{m}) \propto \exp\left[-\frac{1}{2}(\mathbf{d}-\mathbf{g}(\mathbf{m}))^\top \mathbf{C}_{\text{d}}^{-1}(\mathbf{d}-\mathbf{g}(\mathbf{m}))\right], \tag{8}$$

leading to a posterior of the form:

$$p(\mathbf{m} \mid \mathbf{d}) \propto \exp\left[-\frac{1}{2}\Phi(\mathbf{m})\right], \tag{9}$$

where $\mathbf{C}_{\text{d}}$ and $\mathbf{C}_{\text{m}}$ are the data and model covariance matrices, respectively, and $\mathbf{g}(\mathbf{m}) = \left[\mathbf{\Delta T}(\mathbf{m})^\top \; \mathbf{\Delta \rho_a}(\mathbf{m})^\top\right]^\top$ is the coupled thermal electrical forward operator. One can see the solution flowchart in Fig. 3.

In the context of an E-TRT, evaluating the likelihood requires computing $\mathbf{g}(\mathbf{m})$, which is computationally expensive. Sampling-based methods such as Monte Carlo therefore become impractical. Alternatively, under the assumptions of multivariate normality and mild non-linearity of $\mathbf{g}(\mathbf{m})$, the posterior is fully characterized by its mean and covariance. The mean corresponds to the maximum a posteriori (MAP) model, obtained by maximizing the posterior distribution or, equivalently, by minimizing the cost function. For the E-TRT, the cost function is

$$\begin{aligned}\Phi(\mathbf{m}) &= \Phi(\mathbf{m})_T + \Phi(\mathbf{m})_{\rho_a} + \Phi(\mathbf{m})_{\text{prior}} \\ &= (\mathbf{\Delta T}(\mathbf{m}) - \mathbf{\Delta T})^\top \mathbf{C}_T^{-1}(\mathbf{\Delta T}(\mathbf{m}) - \mathbf{\Delta T}) \\ &\quad + (\mathbf{\Delta \rho_a}(\mathbf{m}) - \mathbf{\Delta \rho_a})^\top \mathbf{C}_{\rho_a}^{-1}(\mathbf{\Delta \rho_a}(\mathbf{m}) - \mathbf{\Delta \rho_a}) \\ &\quad + (\mathbf{m} - \mathbf{m}_0)^\top \mathbf{C}_m^{-1}(\mathbf{m} - \mathbf{m}_0),\end{aligned} \tag{10}$$

where $\Phi(\mathbf{m})_T$ is the temperature misfit, $\Phi(\mathbf{m})_{\rho_a}$ is the ER misfit, $\Phi(\mathbf{m})_{\text{prior}}$ is the prior term. The matrices $\mathbf{C}_T$ and $\mathbf{C}_{\rho_a}$ represent the data covariance for temperature and ER, respectively, and $\mathbf{C}_m$ describes the prior uncertainty. Because the temperature and ER datasets are assumed independent, the full data covariance matrix is block diagonal, $\mathbf{C}_d = \text{diag}(\mathbf{C}_T, \mathbf{C}_{\rho_a})$. The MAP model is obtained with a Gauss–Newton method, which iteratively updates the model as

$$\begin{aligned}\mathbf{m}_{n+1} =& \mathbf{m}_n - \mu_n\left(\mathbf{J}_n^T \mathbf{C}_d^{-1} \mathbf{J}_n + \mathbf{C}_m^{-1}\right)^{-1} \\ & \left[\mathbf{J}_n^T \mathbf{C}_d^{-1}\left(\mathbf{g}(\mathbf{m}_n) - \mathbf{d}\right) + \mathbf{C}_m^{-1}\left(\mathbf{m}_n - \mathbf{m}_{\text{prior}}\right)\right],\end{aligned} \tag{11}$$

where $\mu_n \leq 1$ is a step size and $\mathbf{J}_n$ is the Jacobian of $\mathbf{g}(\mathbf{m}_n)$.

Once the MAP model is obtained, the posterior covariance matrix is computed as (Tarantola, 2005)

$$\mathbf{C}_m' = (\mathbf{J}_T^\top \mathbf{C}_T^{-1} \mathbf{J}_T + \mathbf{J}_{\rho_a}^\top \mathbf{C}_{\rho_a}^{-1} \mathbf{J}_{\rho_a} + \mathbf{C}_m^{-1})^{-1}, \tag{12}$$

where $\mathbf{J}_T$ and $\mathbf{J}_{\rho_a}$ are the temperature and resistivity change Jacobians at the MAP solution $\mathbf{J}_{MAP} = [\mathbf{J}_T^\top \, \mathbf{J}_{\rho_a}^\top]^\top$. The uncertainties of the thermal parameters are then estimated from the 95% confidence intervals (Aster et al., 2018):

$$\mathrm{conf} = \pm 1.96\sqrt{\mathrm{diag}(\mathbf{C}'_m)}. \tag{13}$$

Accurate estimation of the posterior and its confidence intervals requires appropriate definitions of the data covariance matrices and the prior. For the ER correlation matrix $\mathbf{C}_{\rho_a}$, we assume independent and normally distributed measurement errors, so $\mathbf{C}_{\rho_a}$ is diagonal with entries $\sigma^2_{\rho_a}$. This assumption neglects spatial or temporal correlations, which may slightly underestimate the confidence intervals. For the temperature covariance matrix, we account for temporal autocorrelation following Pasquier and Marcotte (2020) using an exponential model:

$$\mathbf{C}_T(h) = \sigma_T^2 e^{-\frac{h}{a}}, \tag{14}$$

where a is the correlation range, σ_T^2 is the sill and h is the time lag between measurements.

The prior $\mathbf{C}_m$ allows incorporation of prior knowledge about the model to guide the inversion. In this study, the inverse problem is sufficiently well-posed that an uninformative prior $\mathbf{C}_m^{-1} \approx 0$ is adequate.

It is worth noting that we adopted a parametric inversion approach to estimate the three thermal parameters directly, rather than performing a spatial inversion of the electrical resistivity data, which is the conventional approach in geophysics. This choice is motivated by the limitations of spatial regularization, which tends to smooth resistivity distributions and thus restricts the accurate resolution of hydrogeological and heat transport parameters (Hermans et al., 2012).

3. Synthetic experiment

To assess the performance of the coupled E-TRT model, a synthetic noiseless simulation was conducted. A constant heat flux of 115.6 W/m was applied for 72 h, a typical duration that provides sufficient accuracy for estimating k (Spitler and Gehlin, 2015; Choi et al., 2018). The thermal properties of the bedrock were selected to reflect the values recovered in the field experiment (Section 4), with $k = 2.75$ W/m/K, $C_s = 2.5$ MJ/m^3/K and $m = 0.035$ °C^{-1}. Given the resulting characteristic time $t_b = 8.6$ h, the data after 12 h were used for both temperature and ER measurements to avoid short-term modelling errors.

The initial temperature and electrical properties of the ground and water, as well as the heating applied and the sampling rate for both datasets, are presented in Table 1. Values are chosen to be close to those at the experimental site. Direct measurements of water electrical resistivity were replaced with a constant electrical resistivity $\rho_{w,0}$. The following sections present the modelled resistivity and temperature data and the inversion accuracy. A more in-depth analysis is provided in the appendices. Appendix B compares the sensitivities of temperature and ER measurements; Appendix C examines the influence of ER survey design on parameter recovery; Appendix D assesses the effect of heat injection rate error; and Appendix E investigates the impact of borehole water resistivity.

3.1. Modelled thermal and electrical perturbations

Fig. 4(a) illustrates the resulting thermal perturbation after 72 h of heating causing electrical resistivity variations in the bedrock (bottom). The temperature variation of 14 °C is greatest at the borehole wall and decreases radially. Fig. 4(b) illustrates the resulting electrical model. Due to the inverse linear relationship between temperature and resistivity (Eq. (4)), the largest decrease from the reference rock resistivity $\rho_{r,0} = 15$ Ω m is concentrated within 1 m near the borehole, gradually approaching the reference value at greater distance. This underlines the importance of using high-resolution near-borehole ER measurements.

The temperature data are directly measured in the SCW via a probe and the ER data are obtained from increasing the spacing between active electrodes, located in the borehole. The resulting data are presented in Fig. 4(d). The ER response corresponds to a decrease of $\Delta\rho_a$ with time and is solely temperature-dependent, as the resistivity of the water inside the SCW remains constant. The magnitude of the decrease in $\Delta\rho_a$ is electrode-spacing dependent and can be compared to temperature variations at different radii, shown in Fig. 4(c). Indeed, electrode spacing plays a key role, as smaller spacings sample a more localized volume near the borehole, where temperature variations are greatest, resulting in a stronger apparent resistivity change. In contrast, larger spacings integrate over a broader volume farther from the borehole, where temperature changes are less pronounced, leading to a weaker electrical response. The apparent resistivity variation reaches 2.67 Ω m, for an initial bedrock resistivity of 15 Ω m. Although the latter seems modest, it corresponds to a 17.8% change in ρ_a.

Table 1

Properties and survey parameters used in the synthetic and experimental E-TRT models.

Parameter	Units	Synthetic	Experimental
T_0	°C	10	11.5
$\rho_{\mathrm{r},0}$	Ω m	15	15
$\rho_{\mathrm{w},0}$	Ω m	2	2
r_b	m	0.0825	0.0825
$t_{\max}$	h	72	256
q	W/m	115.6	115.6
Δt_T	min	10	10
Δt_ρ	h	4	2–4
Δe	m	0.25	0.25
N_e	–	8	8

3.2. Parameter estimation

Due to the respective sensitivities of ER and temperature data to the three thermal parameters demonstrated in Appendix B, their joint use may provide complementary information, and therefore additional constraints, on C_s, k and m. In this synthetic study, noiseless ER and temperature data are used to evaluate whether the solution, the true thermo-electrical parameters ($C_s = 2.5$ MJ/m^3/K, $k = 2.75$ W/m/K and $m = 0.035$ °C^{-1}) can be reliably recovered. The initial model supposes good knowledge of k, along with standard values set for C and m, set to $k = 2.6$ W/m/K, $C_s = 2.0$ MJ/m^3/K and $m = 0.018$ °C^{-1}. Inversions were performed using temperature data alone (the TRT dataset) and then using the full E-TRT dataset with Eq. (11). The TRT inversion excluded m due to its insensitivity. Both approaches converged within 10 iterations, after which the parameter updates became negligible, and the solution recovered the true thermal parameters. This indicates that local gradient-based inversion can be applied to process both TRT and E-TRT in a perfect scenario (no noise, perfect physics).

3.3. Uncertainty estimation

A careful analysis of noise sensitivity and uncertainty is required to assess the gain of the E-TRT over the TRT under realistic conditions. To this end, the confidence intervals from the posterior covariance matrix were calculated at the MAP estimate using Eq. (13) with data covariance matrices based on parameters reported in Table 2. The MAP uncertainty depends on the covariance matrix and a linear approximation around the solution. To confirm the MAP results, two complementary uncertainty estimations are presented: a Monte-Carlo analysis (MC) and a grid-search of the misfit around the solution.

For the Monte-Carlo analysis, data were generated by perturbing the MAP model predictions with random Gaussian noise following $\mathbf{C}_d$, and the inversion was performed for 8 iterations using the MAP thermal parameters perturbed according to $\mathbf{C}_m$ as the initial model. The latter was defined from a Gaussian approximation of a uniform distribution bounded within typical parameter ranges: [1 – 5.0] W/m/K for k, [2.0

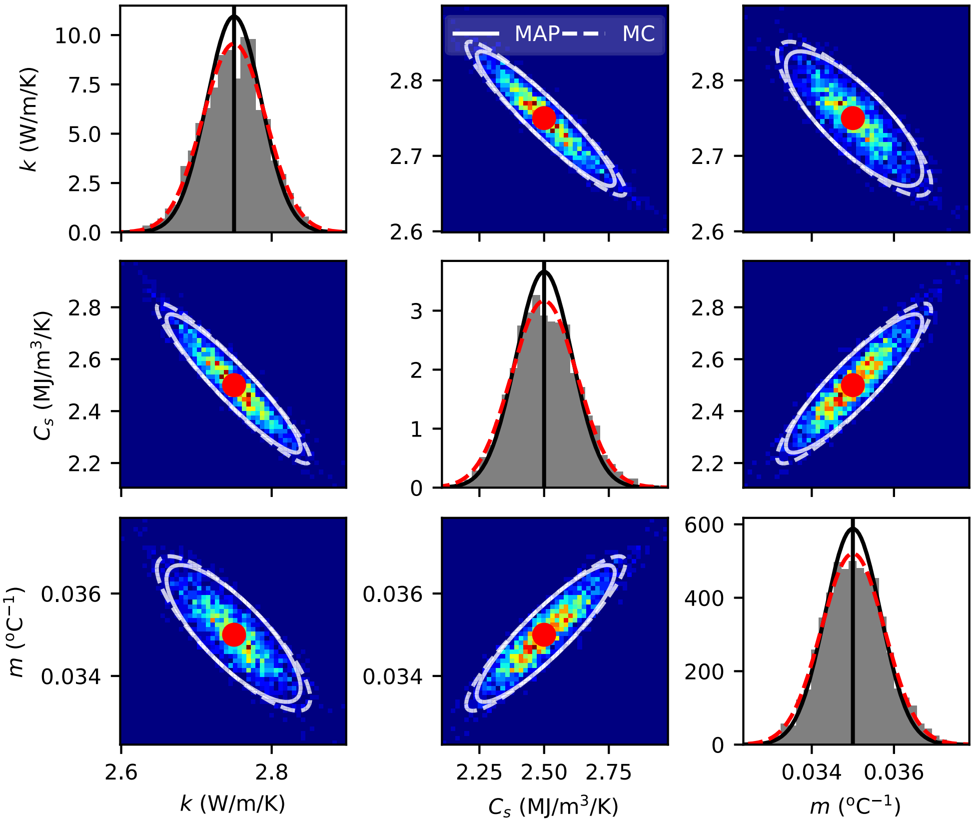

Fig. 5. Monte-Carlo (MC) analysis of the E-TRT. Results from 2000 simulations are shown, with the true model indicated by the red dot. The 95% covariance ellipsoids are plotted for the MC and MAP estimates.

Table 2
Measurement uncertainties and covariance model parameters obtained in the experimental E-TRT and used in the synthetic case.

Error	Value
Measurement error	
σ_ρ (Ω m)	0.092
σ_T (°C)	0.26
Exponential covariance model	
Correlation range a (h)	7
Temperature variance σ_T^2	0.013

Table 3
Absolute and relative 95% uncertainty widths for thermal parameters using MAP, misfit-based bounding box (Box) and Monte-Carlo (MC) approaches under TRT and E-TRT conditions on the synthetic case.

Param.	Method	TRT	E-TRT
k (W/m/K)	MAP	0.21 (7.5%)	0.07 (2.6%)
	MC	0.19 (6.9%)	0.08 (3.0%)
	Box	0.41 (7.5%)	0.09 (3.3%)
C_s (MJ/m^3/K)	MAP	0.63 (25.4%)	0.21 (8.5%)
	MC	0.59 (23.4%)	0.25 (9.9%)
	Box	1.29 (25.8%)	0.31 (12.4%)
m (°C^{-1})	MAP	–	0.00133 (3.8%)
	MC	–	0.00150 (4.3%)
	Box	–	0.0020 (5.7%)

– 3.5] MJ/m^3/K for C_s and [0.018 – 0.03] °C^{-1} for m. A total of 10 000 simulations were performed for the TRT, and 2000 simulations for the E-TRT due to computational cost.

For the grid-search of the misfit, we computed the misfit on a regular grid (Δk = 0.03 W/m/K, ΔC_s = 0.03 MJ/m^3/K and Δm = 0.00017 °C^{-1}). For a multivariate normal distribution, the misfit should follow a χ^2 distribution with n degrees of freedom (Aster et al., 2018), corresponding to the number of parameters ($n = 2$ for TRT and $n = 3$ for E-TRT). The 95% confidence region is then obtained by the isocontour of the 95th percentile of the χ^2 distribution Δ^2, given by $\Phi(\mathbf{m}) \leq \Phi(\mathbf{m}_{\mathbf{est}}) + \Delta^2$, where $\mathbf{m}_{\mathbf{est}}$ are the estimated model parameters. For the following, we report the bounding box of this region, which serves as the most conservative estimation of the confidence interval. Note that the misfit computation takes full account of the non-linearity of $\boldsymbol{g}(\boldsymbol{m})$, but that the isocontour criterion assumes linearity. This is thus a mixed approach between MAP ellipsoid and pure MC.

Confidence intervals obtained by the three methods are reported in Table 3. Using temperature data alone and the MAP covariance, k is resolved with an 7.5% uncertainty, while C_s is resolved with a 25.4% uncertainty. The addition of ER data improves resolution of k to 2.6%, and of C_s to 8.5%, a substantial improvement. Moreover, the E-TRT allows the estimation of m within 3.8% uncertainty. The MAP, MC, and the bounding box methods yield comparable uncertainties, supporting the conclusion that E-TRT reduces uncertainty by a factor of 3 over standard TRT.

The discrepancies between the uncertainty estimates obtained with the three methods are small and consistently support the improved performance of the E-TRT. The bounding box shows the highest uncertainty estimation, as it includes parameter space volume outside of the actual confidence region. Relative to the MC, the MAP covariance slightly underestimates the uncertainty for the TRT (by 0.6% for k and 2.0% for C_s) and overestimates the uncertainty for the E-TRT (by 0.4% for k, 1.4% for C_s and 0.5% for m). The suitability of the linear MAP approximation is further confirmed by Fig. 5, comparing the MAP and MC posterior distributions. The posterior distribution sampled with MC shows that all three parameters are normally distributed, with marginals closely reproduced by the MAP ellipsoid. Hence, the non-linearity is mild and the MAP covariance approximation is appropriate;

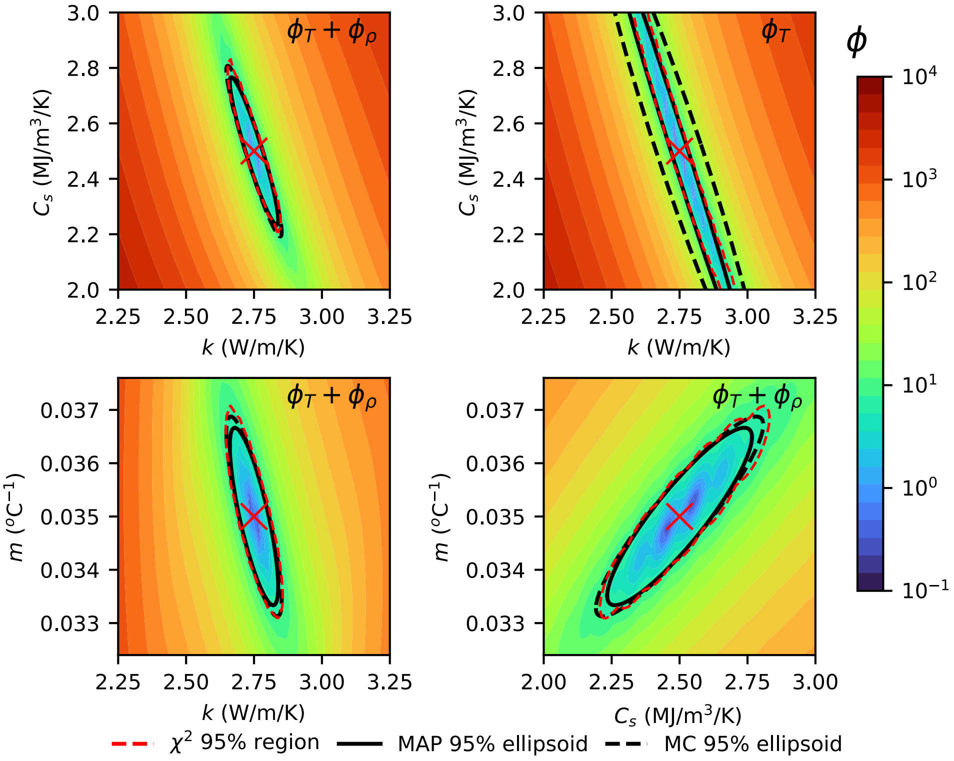

Fig. 6. Visualization of misfit Φ in the (k, C_s), (k, m) and (C_s, m) parameter plane. The true solution, C_s = 2.5 MJ/m^3/K, k = 2.75 W/m/K and m = 0.035 °C^{-1}, is marked with a red X. The top-right panel displays Φ_T, only. The corresponding MAP ellipsoids and misfit confidence regions are plotted.

further analyses therefore rely primarily on this approach due to its lower computational cost.

Fig. 6 illustrates the resulting misfit plot in two-dimensional parameter planes (k, C_s), (k, m) and (C_s, m), while minimizing over the third parameter. The TRT misfit plot (k, C_s) reveals a narrow confidence region valley spanning between 1.95 and 3.24 MJ/m^3/K (outside of the plot) around the solution, indicating that multiple combinations of k and C_s can reproduce the observed temperature of a TRT when the ICS model is used. This elongated shape of the misfit is consistent with previous findings and illustrates the low confidence on C_s (Li and Lai, 2012; Zhang et al., 2015). In comparison, the E-TRT (k, C_s) plane shows a much narrower misfit valley, further confirming that ER data is more discriminative with respect to C_s. In the (k, m) plane, the misfit shows that k and m are almost uncorrelated, illustrated by a near-vertically aligned confidence region. In contrast, the (C_s, m) plane shows a more gradual variation, reflecting a weaker constraint on the solution. The confidence region is oriented at approximately a 45-degree angle, indicating a correlation between both parameters. This suggests that variations in C_s and m, both volumetric properties, may compensate for each other in the model response.

In conclusion, these results confirm that the MAP covariance captures the local behaviour of the cost function for both TRT and E-TRT datasets and provides a reliable estimation of the 95% confidence interval. Most importantly, they demonstrate that the E-TRT indeed substantially reduces the uncertainty of C_s and enables reliable estimation of m.

4. Experimental application to Varennes study site

The value of complementing conventional TRTs with ER measurements, particularly on the recovery of C_s and m, has been explored through synthetic modelling. Building on these findings, the following section presents the results of an experimental E-TRT conducted between October 8 and November 4th, 2024.

4.1. Site description

The E-TRT was carried out on an SCW at the mobile geothermal laboratory in Varennes, Canada. Fig. 2(a) presents pictures of the inside and outside of the laboratory. Beaudry et al. (2018) conducted a comprehensive characterization of the site, including geological identification of the bedrock and thermal conductivity from probe measurements from borehole cuttings and a thermal response test. The 215 m deep SCW, with a 165 mm diameter, is located in the Nicolet Formation of the Lorraine Group, which at the site consists of fine-grained sedimentary rock interbedded with sandstone, siltstone, and limestone. Approximately 10 m from the SCW, a 150 m reinjection well (IW) injects the bleed water into the aquifer. The laboratory is equipped with a data acquisition system that measures LWT and EWT, flow rates and heating power generated by a 24 kW nominal water heater as seen in Fig. 2(a). The SCW geometry enables pumping at a depth of 18 m and reinjection near the bottom of the well. The rejection pipe is screened for 5 m. Additional pressure sensors were added in the SCW and in the reinjection well to monitor water levels. The SCW was equipped with a DTS calibrated with a water bath and a temperature sensor. A 10-minute measuring interval was chosen, with a spatial resolution of 0.5 m, comparable to typical sampling intervals for distributed TRTs that range from 1 min to 60 h (McDaniel et al., 2018).

4.2. Thermal response test

The thermal response test lasted 21 days. During the recirculation, heating, and bleed phases, both LWT and EWT were recorded. For the recovery phase, only temperature data along the SCW were collected using DTS. The undisturbed ground temperature was also measured using DTS. The recirculation phase lasted 48 h. In the heating phase, an average heating power Q of 24.01 kW was applied for 256 h. This is by far longer than conventional TRT and was done to maximize thermal perturbation in the bedrock. The heating power is obtained from the

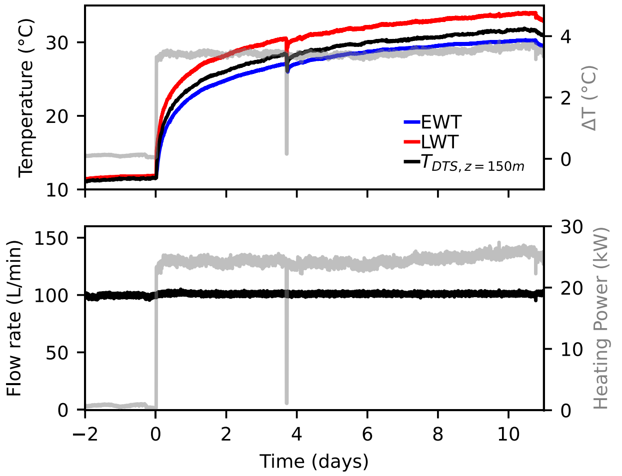

Fig. 7. Thermal response test data. Top: Inlet and outlet temperatures alongside the DTS temperature at the depth of the cable. Bottom: Measured flow rates and heating power.

temperature difference $\Delta T = EWT - LWT$ using $Q = \Delta T\dot{V}(\rho C_p)_w$, where $\dot{V}$ is the pumping rate and $(\rho C_p)_w$ is the water volumetric heat capacity (Beaudry et al., 2018). The higher heating power than the water heater's capacity is caused by additional heating from the pump. This is equivalent to a unit heat load q of 115.6 W/m when using an effective length of 208 m, accounting for the depth of the water table and the screened reinjection pipe, and an average flow rate of 105.60 L/min. During the bleed phase, heating was maintained and a 3.25 L/min bleed flow rate was applied. For the recovery phase, both heating and water recirculation were stopped. While it is typical to continue water recirculation during recovery, we chose otherwise to assess the impact of water circulation on the electrical data. Following the cessation of heating and recirculation, the DTS system continued to collect temperature data for an additional 5 days to monitor the recovery process. The evolution of inlet and outlet temperatures, flow rates, and heating power during the TRT are summarized in Fig. 7.

4.3. *Electrical measurements*

The ER measurements were performed with a 32-electrode cable at 25 cm spacing, shown in Fig. 2(c). The cable was installed in the SCW at a depth of 150 m, in a 20 m-thick bed of relatively homogeneous mudshale (Beaudry et al., 2018). Particular care was required during installation, as the 165 mm-diameter borehole already contained a 51 mm reinjection pipe and an optical-fibre cable. The surface electrodes were positioned 40 m horizontally from the borehole to meet the required minimum distance of 155 m, as specified for this configuration (Loke, 2001). The protocol was designed to minimize acquisition time and consisted of 335 measurements with up to four stacks for a variance smaller than 1% and took about 20 min. Current was injected at every 5th electrode and the potential was measured at the remaining electrodes, resulting in an electrode spacing ranging from 0.25 to 7.75 m. This setup ensured that all potential measurements for a single injection electrode were taken consecutively, minimizing the time between measurements. Data acquisition was carried out using the ABEM Terrameter LS. The Terrameter LS was installed inside the laboratory and connected to both a power outlet and a computer, as shown in Fig. 2(a). Automated measurements were conducted at two-hour intervals, and the acquisition interval was extended to four hours after the sixth day of heating to minimize electrode corrosion.

Due to the sensitivity of electrical measurements to the groundwater in the SCW, water conductivity was carefully monitored throughout the TRT using two different probes. A multiparameter probe (Hanna 98194) was placed inside the mobile laboratory within a parallel water circuit and housed inside a thermally insulated Faraday cage, with a sampling interval of 5 min. A water conductivity data logger (LTC probe) was positioned 1 metre below the pump intake in the SCW, with a sampling interval of one minute. Groundwater samples were taken at every field visit. The electrical conductivity of each water sample was measured at 25 °C to validate the probe readings. Two water samples were heated over a temperature range of 11 to 35 °C, during which the electrical conductivity was recorded. A linear regression analysis was performed to establish the site-specific relationship between temperature and groundwater electrolyte conductivity m_f.

4.3.1. *Error estimation*

Estimating the error is essential for field-based electrical measurements. A common approach is the reciprocal error, calculated by interchanging the injection and potential electrodes for each quadripole configuration:

$$|e| = \frac{||R_f| - |R_r||}{2}, \tag{15}$$

where R_f and R_r are the forward and reciprocal resistances, respectively (Tso et al., 2017). In this study, each protocol included 50 pairs of reciprocal measurements, and a complete reciprocal protocol was conducted at the end of recirculation, heating, bleeding and recovery. For this dataset, the reciprocal error falls below 2% for 98% of the data. To ensure data quality, experimental apparent resistivity ρ_a was filtered by removing measurements with a reciprocal error exceeding 4% and those from identified defective electrodes. Variations $\Delta\rho_a$ were calculated relative to the initial measurements taken before heating. Given the short length of our multi-electrode cable (7.25 m), vertical homogeneity of the rock formation is assumed, meaning that identical spacing at different depths along the cable should yield the same apparent resistivity. Under this hypothesis, ρ_a and $\Delta\rho_a$ were averaged for each electrode spacing to improve accuracy and reduce noise. ER uncertainty was first obtained for each spacing, where a $|e| = 2\%$ error on all filtered ρ_a values was averaged by the number of timesteps N_t and the number of duplicates N_ρ. These duplicates further reduce the error by a factor of $\sqrt{N_\rho}$. The resulting per-spacing error was averaged across all spacings N_e to obtain a single representative uncertainty, expressed as

$$\sigma_\rho = \frac{1}{N_e}\sum_{i=1}^{N_e}\left(\frac{1}{\sqrt{N_{\rho,i}}}\frac{|e|}{N_t N_{\rho,i}}\sum_{j=1}^{N_{\rho,i}}\rho_{a,ij}\right), \tag{16}$$

yielding an uncertainty of $\sigma_\rho = 0.092\ \Omega\,\mathrm{m}$. For the temperature data, the standard deviation of residuals between DTS measurements and the sensor inside the calibration bath provided measurement uncertainty of $\sigma_T = 0.26$ °C. The temperature data were inverted using the ICS, and the residuals were used to obtain the experimental variogram, from which the temperature drop from the power outage was removed. The resulting fit of the exponential model (Eq. (14)) is illustrated in Fig. 8 and results in a sill of 0.013 °C^2 and a correlation range of 7 h. The experimental errors are summarized in Table 2 and were used for parameter estimation in Section 3.

4.4. *Results and discussion*

4.4.1. *Experimental data*

The resulting experimental data during the heating phase are presented in Fig. 9, with the shaded areas around $\Delta\rho_a$ indicating the measurement error. Besides the measurement error described in Eq. (16), the standard deviation from averaging $\Delta\rho_a$ across electrode spacings provides a measure of homogeneity along the cable section. The resulting average variability is 0.2 Ω m, corresponding to 14.7% of the mean $\Delta\rho_a$. This relatively low variability, together with the distinctive temporal trend observed for each spacing, supports the assumption of vertical homogeneity. Spacings greater than 2 m were excluded, as their

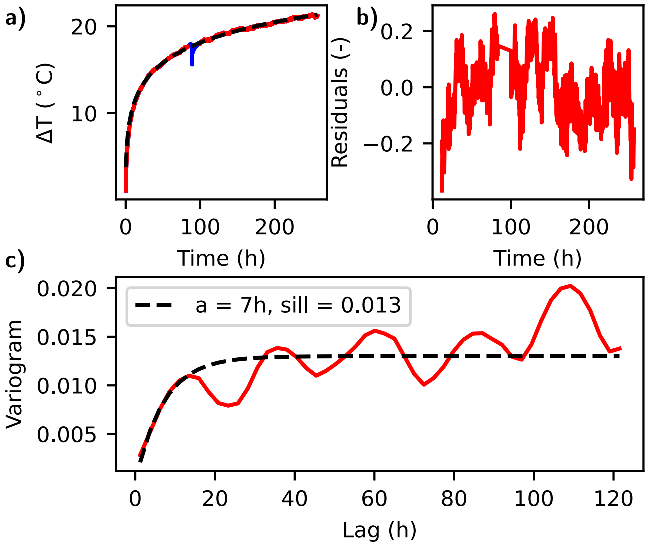

Fig. 8. Temperature residuals modelling. (a) ICS model is fitted to the temperature data. (b) Residuals between model and measurements. (c) Exponential variogram model fitted to the residuals.

Table 4
Measured groundwater conductivity at 25 °C and m_f values for three samples taken at different stages of the thermal response test.

Sample	m_f	σ_{25} (S/m)	ρ_{25} (Ω m)
A – Start of heating	0.0204	0.57	1.77
B – End of heating	0.0194	0.67	1.49

standard deviation exceeded the corresponding $\Delta\rho_a$ values. The data collected during the bleed and recovery phase are not shown here and will not be used for parameter estimation in this paper. The average direct temperature measurements obtained from the DTS between 150 and 158 m in the SCW are presented in Fig. 9(b). There was a small power outage on day 3, noticeable by a decrease in water temperature. Fig. 9(c) displays the water resistivity values measured by the LTC probe, as the Hanna Probe measured similar values with a higher noise level. The blue dots represent the groundwater resistivity at 25 °C from laboratory measurements. The measurements for m_f for samples A and B were taken at the beginning and at the end of heating, respectively, and are presented in Table 4.

During heating, a 20.4 °C increase in groundwater temperature corresponds to a decrease in water resistivity. The electrolytic conductivity is expected to increase and the resistivity to decrease, in proportion to the temperature within this range. As illustrated in Fig. 9, this trend holds except for the first day. Robert et al. (2013) showed that bulk resistivity may diverge from expected temperature–resistivity relationships due to mineral precipitation with temperature increase and chemical disequilibrium between pore water and the formation matrix. Although the recirculation phase homogenizes water properties inside the SCW, this does not imply equilibrium with the adjacent bedrock. The laboratory analysis presented in Table 4 demonstrates that the two samples extracted during the heating process exhibited different conductivities at 25 °C and supports the idea that changes in chemical composition contributed to these differences. This is supported by examining the first 24 h of the ER data, which shows a decrease in apparent resistivity, followed by an increase and then a decrease at 24 h. A similar trend was also observed by Robert et al. (2013) on a laboratory column experiment, further supporting the notion that geochemical reactions impacted water resistivity. For these reasons, the first day of heating was excluded from the parameter estimation process, as the numerical model does not account for chemical reactions.

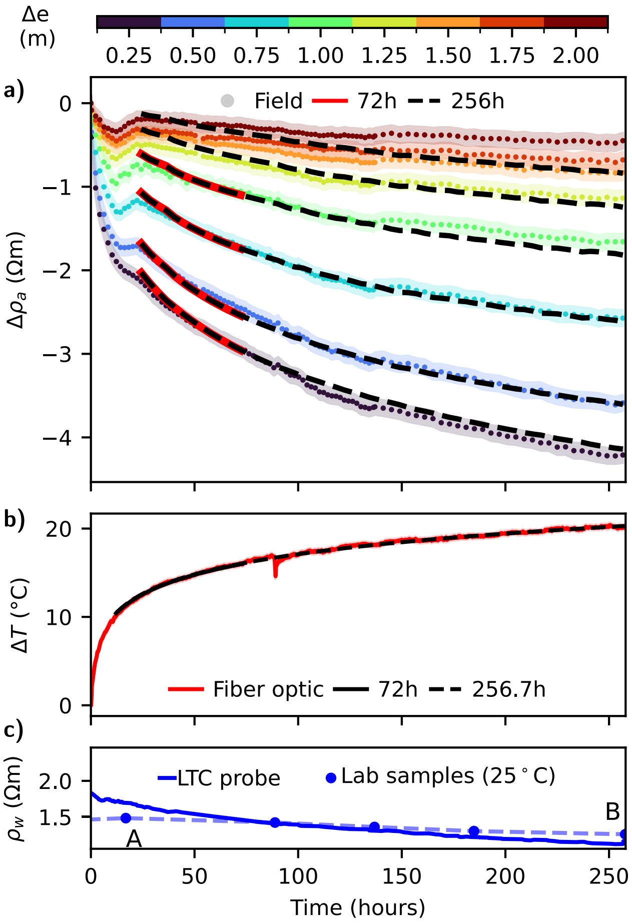

Fig. 9. E-TRT data obtained from the experiment at the Varennes test site, along with the predicted data from the inverted E-TRT solution. (a) Apparent resistivity variation with respect to time for electrode spacings between 0.25 m and 2.00 m. The shaded area shows the measurement error σ_ρ. (b) Average temperature obtained from DTS at the depth of the cable (150.00–157.75 m). (c) Water resistivity measurements obtained from an LTC probe located under the pump intake. The resistivity at 25 °C of the lab samples are shown, and the dashed line gives the specific resistivity interpolated from the samples.

The experimental ER data is comparable to the synthetic results shown in Fig. 4(d), where $\Delta\rho_a$ decreases across all electrode spacings, with the strongest decrease observed at smaller spacings. For the experimental dataset, a maximum decrease of 27.3% is obtained at the 25 cm spacing. This supports that the experimental ER measurements are sensitive to temperature variations in the bedrock. Inverting only for the reference time estimates a bedrock resistivity of 15 $rm\Omega$ m, which aligns with the expected resistivity of shales (Binley and Slater, 2020).

4.4.2. Parameter estimation

The thermal parameters k, C_s and m were estimated using two datasets: the first 72 h of measurements, corresponding to a conventional TRT length, and the full 256-hour dataset. For both durations, the heating phase of the TRT was first interpreted using the first-order approximation of the line-source model using borehole inlet and outlet temperature from Fig. 7 (ILS-1st; see Appendix A). Inversions were performed for both the 72-hour and full datasets. The TRT inversion used DTS temperature data at cable depth 12 h after the start of heating, to avoid short-term modelling errors. The E-TRT inversion includes the ER measurement 24 h after the start of heating, to avoid including data affected by thermo-chemical effects. In addition, the temporal ER data

Table 5
Recovered thermal parameters for survey durations of 72 h and 256 h using three approaches: the first-order approximation of the ILS (ILS-1st), temperature-only TRT inversion, and joint E-TRT inversion. Values in bold are the recovered experimental parameters. MAP-estimated parameters are reported with their 95% confidence intervals. The associated RMSE values are provided for each dataset, with relative RMSE expressed with respect to the recovered parameters.

Parameter	t_{max}	ILS-1st	TRT	E-TRT
k	72	2.70	2.41 ± 0.18	2.68 ± 0.10
(W/m/K)	256	2.74	2.60 ± 0.07	**2.65 ± 0.02**
C_s	72	–	3.27 ± 0.75	2.31 ± 0.29
(MJ/m^3/K)	256	–	2.61 ± 0.28	**2.35 ± 0.09**
m ($\times 10^{-2}$)	72	–	–	3.60 ± 0.17
(°C^{-1})	256	–	–	**3.61 ± 0.04**
RMSE $\Delta\rho_a$	72	–	–	0.092 (5.8%)
(Ω m)	256	–	–	0.083 (4.3%)
RMSE ΔT	72	–	0.077 (0.6%)	0.119 (0.9%)
(°C)	256	–	0.150 (0.9%)	0.154 (0.9%)

Table 6
Absolute and relative 95% uncertainty widths for thermo-electrical parameters using MAP and misfit bounding box (Box) approaches under TRT and E-TRT conditions.

Param.	Method	TRT	E-TRT
k	Box–72	0.26 (9.9%)	0.13 (4.7%)
(W/m/K)	MAP–72	0.18 (6.7%)	0.10 (3.8%)
	MAP–256	0.07 (2.5%)	0.02 (0.9%)
C_s	Box–72	0.83 (35.1%)	0.38 (16.0%)
(MJ/m^3/K)	MAP–72	0.75 (32.1%)	0.29 (12.4%)
	MAP–256	0.28 (11.9%)	0.09 (3.8%)
m	Box–72	–	0.0022 (6.1%)
(°C^{-1})	MAP–72	–	0.0017 (4.7%)
	MAP–256	–	0.0004 (1.3%)

were sampled at 4-hour intervals, as the first 6 days of the experiment were sampled at 2-hour intervals. This adjustment ensures that the contribution of ER measurements remains balanced throughout time.

All four inversions converged within 10 iterations, after which the parameter updates became negligible. Fig. 9 plots the modelled data at the optimum against the experimental measurements. For the E-TRT inversion, the model fails to reproduce the measured $\Delta\rho_a$ at larger spacing for early times. As a result, only four spacings between 0.25 m and 1 m were kept for the 72-hour case, and six spacings between 0.25 m and 1.5 m were kept for the full case. This selection allowed both datasets to fit the ER data within measurement error $\sigma_\rho = 0.092$ Ω m.

The recovered thermo-electrical parameters, along with the temperature and ER data misfits, are presented in Table 5. Using the ILS-1st, the recovered equivalent thermal conductivity is 2.70 W/m/K for the 72-hour and 2.74 W/m/K for the 256-hour TRT. These values are consistent with previous site-specific estimates, which range between 2.74 and 2.78 W/m/K (Beaudry et al., 2018). The TRT recovered k values are slightly lower than those recovered via ILS-1st and vary greatly between the two TRT survey durations. As shown in Appendix C (Fig. 12), confidence improves with longer TRT, meaning that C_s obtained from the longer survey should be more accurate. The unusually long 256-hour TRT also serves to provide a more accurate reference than the standard 72-hour TRT, against which E-TRT values can be compared. As reported in Table 5, both E-TRT MAP estimates fall closer to the 256-hour TRT values, supporting the conclusion that E-TRT improves accuracy compared to a standard TRT of the same duration. This will be discussed in more detail in the next section on uncertainty estimation.

For the remainder, the 256-hour E-TRT MAP estimates are chosen as the representative solution, as they exhibit the tightest confidence intervals. The recovered thermal parameters for the Varennes site are $k = 2.65$ W/m/K, $C_s = 2.35$ MJ/m^3/K, and $m = 0.0361$ °C^{-1}. In SCWs, recirculation can induce groundwater flow between the borehole wall and the surrounding bedrock, even in the absence of bleed (Yuill and Mikler, 1995; Rees et al., 2004; Robert et al., 2022). Consequently, the recovered thermal parameters can be interpreted as effective values, as is usually the case for TRTs (Spitler and Gehlin, 2015), and are representative of the instrumented section of the cable. Compared with previous studies at the site by Beaudry et al. (2018), k is slightly below the equivalent range of 2.74–2.78 W/m/K, but remains within the broader interval of 2.2–2.9 W/m/K measured by drill cuttings at similar depths. This may also highlight the difference between the borehole equivalent k and local values. As expected, the recovered C_s differs from the 2.07 MJ/m^3/K used by Beaudry et al. (2018), which was based on typical rock properties. The SCW is located within the Nicolet Formation, which at the site and at the depth of the cable, is composed of mudshales. Accordingly, the estimated C_s falls within the expected range for shales (2.26–2.98 MJ/m^3/K) (Sundberg, 1988). The recovered value of m exceeds the ratio between temperature and electrolytic conductivity m_f measured on groundwater samples (0.0194–0.0206; see Table 4). This is consistent with the high clay content of mudshales, as m falls within the higher range expected for clay-rich rocks (0.021–0.28) °C^{-1} (Kristinsdóttir et al., 2010; Nono et al., 2020).

4.4.3. *Uncertainty estimation of the recovered parameters*

To assess the uncertainty of the recovered parameters, the 95% confidence intervals are calculated from the covariance around the MAP (Eqs. (12)–(13)), along with the bounding box of the 95% confidence region of the gridded misfit. Results are reported in Table 6 and displayed in Fig. 10. Note that the bounding box estimate was only calculated for the 72-hour dataset, as the misfit confidence region fell under the grid resolution for the 256-hour dataset. As shown in Fig. 10, the MAP ellipsoids agree well with the confidence region for the TRT and E-TRT, indicating that MAP-based uncertainties remain reliable for experimental data. The misfit values diverge from those obtained in the synthetic case (Fig. 6) due to the presence of measurement noise and modelling error.

A marked reduction in uncertainty is observed for both TRT and E-TRT when extending the survey from 72 to the 256 h, in accordance with the analysis presented in Appendix C (Fig. 12). In both the 72-hour and full-duration cases, the inclusion of ER data substantially reduces the uncertainty of k and C_s. While k is already constrained within 10% by the 72-hour TRT, Table 6 shows a twofold reduction for both durations. For C_s, the improvement is substantial, decreasing from 24.2% to 12.4% for the 72-hour E-TRT and 11.0% to 3.8% for the full-duration E-TRT. For m, the uncertainty is already 4.7% for the 72-hour E-TRT, meaning that it is well resolved.

To better understand the discrepancies in the estimated thermal parameters observed in (Table 5), we analyse the gridded misfit shown in Fig. 10 following the methodology described previously. In the (k, C_s) plane (top-right), the TRT confidence region appears as an elongated valley in the direction of C_s, extending beyond the maximum grid value of 3.5 MJ/m^3/K. The confidence region encompasses the TRT solutions for both survey durations, along with the estimate from Beaudry et al. (2018). This suggests that the discrepancy with the k estimate of Beaudry et al. (2018) is not necessarily linked to heterogeneity along the SCW, but rather to the poor constraint of C_s. Indeed, tight bounds on k for a TRT can only be achieved by imposing a strong prior on C_s. While this is common practice, such a strong prior risks biasing the solution if it is incorrect and may lead to a false sense of accuracy. In the case of Beaudry et al. (2018), the prior C_s=2.07 MJ/m^3/K led to a high k value due to the strong anti-correlation of the TRT misfit shown in Fig. 10. In contrast, the E-TRT misfit (top-left) reveals a better-defined confidence region, which includes both E-TRT estimates, the full dataset TRT solution, and the estimate from Beaudry

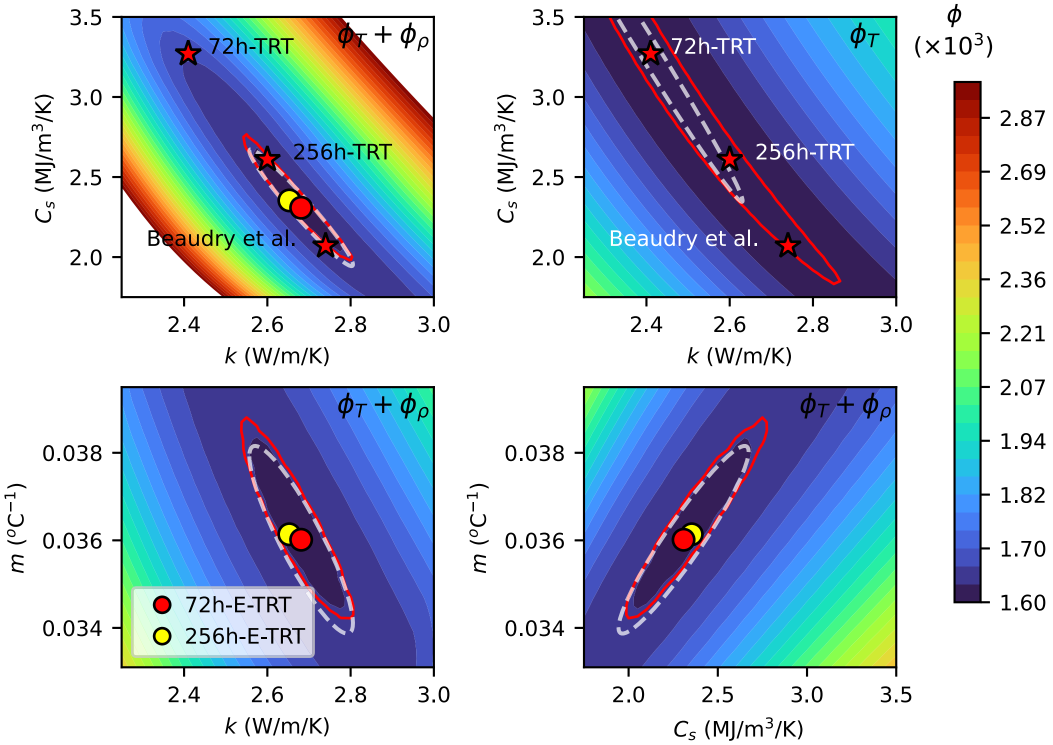

Fig. 10. Visualization of the misfit Φ for the 72-hour survey in the (k, C_s), (k, m) and (C_s, m) parameter planes. The top-right panel displays the Φ_T of temperature data only. The corresponding MAP ellipsoids (dashed white line) and misfit confidence regions (red) are plotted, together with the parameter estimates from the 72-hour and 256-hour TRT and E-TRT, as well the values from Beaudry et al. (2018).

et al. (2018). It excludes the 72-hour TRT MAP solution but falls within its 95% confidence region, highlighting the risk of relying solely on a single best-fit value and the advantage of the Bayesian inference framework.

On a final note, our uncertainty estimates compare favourably to those reported in the literature. Pasquier and Marcotte (2020) and Jacques and Pasquier (2023) estimate C_s using correlated temperature residuals and Bayesian inference of conventional TRT data and recovered uncertainties of 16.3% and 14%, respectively. These uncertainties are slightly lower than those recovered from TRT data. However, the latter was sampled at 10-minute intervals, while Pasquier and Marcotte (2020) recommends using a minimum sampling rate of 30 s for an accurate estimation of heat capacity.

5. Conclusion

This study introduces and validates the Electrical Thermal Response Testing (E-TRT) as a novel field methodology for geothermal characterization, demonstrating that integrating electrical resistivity geophysical measurements into a conventional TRT substantially improves the estimation of the thermal conductivity k and volumetric heat capacity C_s. By incorporating spatially sensitive geophysical information and a robust Bayesian inversion framework, E-TRT reduces parameter trade-offs and provides more reliable uncertainty quantification than standard TRT approaches. Moreover, its installation does not alter the operation of a standard TRT and requires only a minor increase in field time, limited to the deployment of a multi-electrode cable and the instrumentation required to measure temperature and water electrical conductivity at the cable depth.

A major contribution of this work is the demonstrated breakthrough in resolving C_s, a parameter that has historically been poorly constrained by conventional TRTs. C_s governs both the short-term transient response of the GHE (Huang et al., 2020) and its long-term response (Li et al., 2019). Accurate estimation of C_s therefore improves modelling of the GHE temperature dynamics during intermittent operation, which has been shown to enhance the thermal performance of several types of GHEs (Jalaluddin and Miyara, 2012; Gao et al., 2010). It also improves predictions of the long-term ground temperature drift under unbalanced loads, which influences long-term performance (Koohi-Fayegh and Rosen, 2018). Both synthetic and field results confirm that the E-TRT allows for a substantial reduction in uncertainty by approximately 50 to 70% for C_s. In addition, this study presents the first reliable in-situ field-scale estimation of the temperature–resistivity coupling parameter m, offering a practical alternative to laboratory-based measurements (Hermans et al., 2012; Giordano et al., 2017; Comina et al., 2019) and core-scale methods (Kristinsdóttir et al., 2010; Nono et al., 2020).

A 256-hour experimental E-TRT on a SCW validated these results and demonstrated the applicability of the E-TRT under realistic field conditions. The addition of ER data reduced the solution space, stabilized parameter estimates across survey durations, and yielded values consistent with prior site studies and expected lithological ranges.

The present work constitutes a proof of concept applied locally at a single depth of the borehole. The E-TRT could be extended to cover the entire SCW by placing a cable with bundled electrodes along its length to obtain section-wise electrical monitoring. Alternatively, since measurement frequency appears to have a limited influence on the ER sensitivity to C_s, a single diagraphy could be conducted at the end of the recirculation and heating phase.

In this fashion, the thermal parameters could be recovered for different sections of the SCW to quantify subsurface heterogeneity. Finally, the E-TRT framework could be adapted to a closed-loop GHE using an equivalent radius (Fujii et al., 2009).

Nomenclature

Acronyms	
DTS	Distributed temperature sensing
DC	Direct current
ERT	Electrical resistivity tomography
ER	Electrical resistivity
EWT	Entering water temperature
E-TRT	Electrical thermal response test
GHE	Ground heat exchanger
ICS	Infinite cylindrical source
ILS	Infinite line source
IW	Injection well
LWE	Leaving water temperature
MAP	Maximum a posteriori
MC	Monte Carlo
PVC	Polyvinyl chloride
RMSE	Root mean square error
SCW	Standing column well
TRT	Thermal response test
Symbols	
α	Thermal diffusivity (m^2/s)
Δ	Difference
δ	Dirac delta distribution
∂	Partial derivative
C_s	Volumetric heat capacity ($J/m^3/K$)
Φ	Cost function
ρ	Electrical resistivity ($\Omega\,m$)
σ	Measurement uncertainty; also used to denote electrical conductivity (S/m) where specified
a	Correlation range (s)
h	Time lag (s)
C_s	Volumetric heat capacity ($MJ/m^3/K$)
k	Thermal conductivity (W/m/K)
q	Unit heating load (W/m)
Q	Heating power (W)
$\dot{V}$	Circulation flow rate (m^3/s)
m	Fractional change in electrical conductivity ($°C^{-1}$)
N	Number
R	Thermal resistance (Km/W)
r	Radius (m)
T	Temperature (°C)
t	Time (s)
V	Electrical potential (V)
p	Probability density function
$\mathbf{m}$	Model parameter vector
$\mathbf{d}$	Observed data vector
$\mathbf{g}$	Forward model operator
$\mathbf{C}$	Covariance matrix
Subscripts	
0	Initial or reference
a	Apparent
b	Borehole
e	Electrode
eq	Equivalent
est	Estimated
f	Fluid
r	Bedrock
w	Groundwater

CRediT authorship contribution statement

Clarissa Szabo-Som: Writing – review & editing, Writing – original draft, Visualization, Software, Methodology, Investigation. **Gabriel Fabien-Ouellet:** Writing – review & editing, Validation, Supervision, Software, Resources, Methodology, Conceptualization. **Philippe Pasquier:** Writing – review & editing, Validation, Supervision, Resources, Methodology, Funding acquisition. **Adrien Dimech:** Writing – review & editing, Validation.

Declaration of competing interest

The authors declare that they have no known competing financial interests or personal relationships that could have appeared to influence the work reported in this paper.

Acknowledgements

The authors would like to thank Maxime St-Jean, Levy Nougoua, Gabriel Dion and Gabrielle Beaudry for their valuable assistance during field investigations. The authors acknowledge the support from partners of the Geothermal Research Chair on the Integration of SCWs in Institutional Buildings, namely Hydro-Québec, the Ministry of higher education of Québec, CSSMI, CSSDM, CSSS, Versa Profiles, Marmott Energies, CanmetEnergy and NSERC. Additionally, we thank the anonymous reviewers and colleagues that provided constructive comments. This work was financed by the Natural Sciences and Engineering Research Council of Canada, Canada through grant number ALLRP 544477-19 and the Canada Graduate Research Scholarship – Master's program (CGS-M, 2024).

Appendix A. Infinite line source

The analytical model most commonly used is the infinite line source by Ingersoll (1954) that describes the temperature variation at a distance r from the centre of the borehole

$$\Delta T(r,t) = \frac{q}{2\pi k}\int_{\frac{r}{2\sqrt{\alpha t}}}^{\infty} \frac{e^{u^2}}{u}\,du, \tag{17}$$

where $\alpha = \frac{k}{\rho C_s}$ is the thermal diffusivity. The temperature at the borehole wall r_b can be approximated using the first-order approximation of the Taylor expansion of the exponential integral

$$\Delta T(r_b,t) = \frac{q}{2\pi k}\left(\ln\left(\frac{4\alpha t}{r_b^2}\right) - \gamma\right). \tag{18}$$

This model is valid for times greater than $t > \frac{5r_b^2}{\alpha}$, where $\gamma = 0.5772$ is Euler's constant. Substituting Eq. (18) into Eq. (2) allows to plot the temperature variation as a function of logarithmic time. By fixing C_s as a representative value of the geological material, a linear regression can be performed in which the slope is linked to k. A primary drawback of this method is that it requires a constant heating power (Pasquier and Marcotte, 2020; Spitler and Gehlin, 2015) and that both C_s and k cannot be evaluated conjointly.

$$\overline{T}_f(t) = \left[T_0 + qR_b - \frac{q\gamma}{4\pi k} + \frac{q}{4\pi k}\ln\left(\frac{4\alpha}{r^2}\right)\right] + \frac{q}{4\pi k}\ln(t) \tag{19}$$

Appendix B. Sensitivity of ER and temperature to thermal parameters

In this section, we discuss the sensitivity of $\Delta\rho_a$ and ΔT to the thermo-electrical parameters, k, C_s and m, based on the synthetic experiment. The sensitivity is estimated using the Jacobian, which linearizes the forward model around the solution. In this context, a higher magnitude indicates that varying the parameter will cause significant changes in the model's response. In contrast, a lower value indicates that the response will remain unchanged, even if the parameter changes. Fig. 11 illustrates the Jacobian matrix evaluated at the solution with respect to C_s ($\partial\Delta\rho_a/\partial C_s$, $\partial\Delta T/\partial C_s$), k ($\partial\Delta\rho_a/\partial k$, $\partial\Delta T/\partial k$) and m ($\partial\Delta\rho_a/\partial m$). The magnitude increases with time for all Jacobians, reflecting the

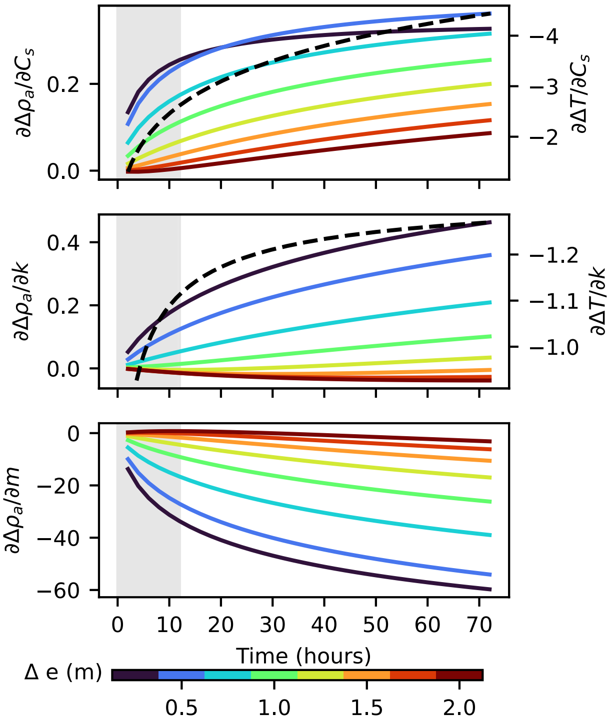

Fig. 11. Jacobian of the electrical and temperature data concerning the estimated thermal parameters k, C_s and m. Electrical data is shown in terms of electrode spacing Δe.

increasing influence of the thermal parameters on the measured signal, likely due to the propagation of the heat plume.

Since electrode spacings Δe have varying sensitivities to temperature variations in the bedrock, they will also show varying sensitivities to the thermal parameters. For $\partial\Delta\rho_a/\partial C_s$, all Δe show similar sensitivity magnitudes, and the sensitivity of wider spacings increases over time, as the thermal front propagates deeper into the formation. The 25 cm spacing plateaus after 24 h, with a similar trend observed for the 50 cm spacing. This stabilization reflects the limited depth of investigation at smaller spacing, which becomes stable once the thermal fronts extend beyond their effective reach. This demonstrates how ER measurement captures volumetric information. Because the 25 cm spacing is more sensitive to temperature near the borehole wall, its behaviour resembles that of $\partial\Delta T/\partial C_s$. However, unlike ER, the temperature sensitivity does not plateau. Indeed, $\partial\Delta T/\partial C_s$ shares a similar shape as ΔT as shown in Fig. 4(d), highlighting that sensitivity to C_s is driven by the increase in temperature at that fixed location. In contrast, $\partial\Delta\rho_a/\partial k$ shows the highest sensitivity for the 25 cm spacing and decreases logarithmically with increasing spacing. This behaviour reflects the strong influence of k on near-borehole temperature gradient and suggests that spatial measurements offer limited additional information. When comparing the 25 cm spacing to $\partial\Delta T/\partial k$, both sensitivities increase over time, but the ER response grows more slowly. Whereas ΔT captures the immediate borehole wall temperature, the volume averaging inherent to ER measurements dilutes the local gradient, thereby smoothing the sensitivity to k. Finally, $\partial\Delta\rho_a/\partial m$ scales directly to $\Delta\rho_a$, shown in Fig. 4(d), consistent with the linear relationship described by Eq. (4). This confirms that the sensitivity to m is primarily driven by the amplitude of the resistivity change itself.

In conclusion, the Jacobian analysis reveals that the volumetric nature of ER monitoring during the TRT provides additional sensitivity to C_s, compared to temperature data alone, and to m.

Appendix C. Influence of E-TRT acquisition design on thermal parameter recovery

The following section evaluates the influence of E-TRT acquisition design. Fig. 12 (top) illustrates the impact of acquisition design on the normalized misfit Φ'_ρ, in the (k, C_s) parameter plane for m fixed at the solution of the synthetic experiment. This normalization allows to highlight the overall sensitivity of the ER dataset, independently of data quantity. The confidence and $\Phi'_\rho = 1$ regions are plotted, the latter marks solutions that fit the ER dataset within σ_ρ. As a result, the Φ'_ρ region is generally broader, since normalization highlights the intrinsic sensitivity of the dataset, rather than its statistical confidence bounds. This distinction emphasizes that summing data with similar sensitivity reduces random error, thereby reducing the confidence region, while Φ'_ρ illustrates the overall leverage of ER measurements. Variations in the shape of these regions reveal how design changes alter ER sensitivity. The first column shows Φ'_ρ (top) and Φ'_T (bottom) for the reference acquisition setup (see Table 1). The other columns show Φ'_ρ for several modifications. Fig. 12 (bottom) illustrates the effect of acquisition design on the MAP 95% confidence intervals of the thermal parameters estimated with TRT and E-TRT. To better understand the role of specific design choices, the following aspects of the E-TRT acquisition design are examined in detail:

Number of electrodes Reducing the number of electrodes shifts the Φ'_ρ=1 and confidence regions towards the TRT regions, lowering the uncertainty gain of the E-TRT as the investigated volume becomes restricted to the borehole vicinity. The E-TRT uncertainty starts to plateau at 8 electrodes, after which the Φ'_ρ regions increase due to the inclusion of insensitive measurements in the normalization.

Electrode spacing Reducing Δe while maintaining a maximum spacing of 2 m increases Φ'_ρ sensitivity and decreases correlation between k and C_s, thereby lowering E-TRT uncertainty. However, decreasing the spacing below the 25 cm reference has little effect on Φ'_ρ, since the information from smaller electrode spacing is already captured in the larger spacing, whereas increasing the electrode spacing leads to a loss in resolution. Nevertheless, reducing Δe improves parameter resolution because measurements with similar sensitivity are added, which further reduces uncertainty.

Temporal sampling Temporal sampling shows negligible effects on Φ'_ρ, as smaller sampling intervals do not substantially increase information over larger intervals. This suggests that a minimal acquisition strategy, such as collecting electrical data only before and after heating, provides valuable constraints on k and C_s. For instance, a single measurement after 30 h still shows a 36% improvement over a standard TRT on C_s uncertainty, and this improvement is essentially the same for k. Still, a smaller sampling interval Δt substantially reduces uncertainty for all parameters (i.e. from ~36% at 30 h to ~74% at 2 h for k and C_s) and should be favoured for high confidence estimation.

Survey length Extending the survey duration substantially reduces the $\Phi'_\rho = 1$ region and the overall TRT and E-TRT uncertainty of all parameters, as heat propagates more deeply in the bedrock. The uncertainty starts to plateau after 5 days. During shorter tests, the E-TRT contributes more effectively to lowering the absolute uncertainty of both k and C_s. With longer durations, the absolute advantage of the E-TRT narrows because TRT uncertainty also improves. Yet the relative advantage remains stable for k and C_s with reductions of ~78% after 10 days and ~74% after 3 days.

Appendix D. Effect of heat injection rate error

Another factor influencing parameter recovery is the uncertainty of the heating power q, as it directly controls the amplitude of heat transfer. To assess its impact, q was incorporated into the synthetic data with an associated measurement uncertainty $\mathbf{C}_q$ defined as a constant. For this purpose, q was included in the estimated parameters with a tight prior, reflecting that it is a measured quantity. The uncertainty of

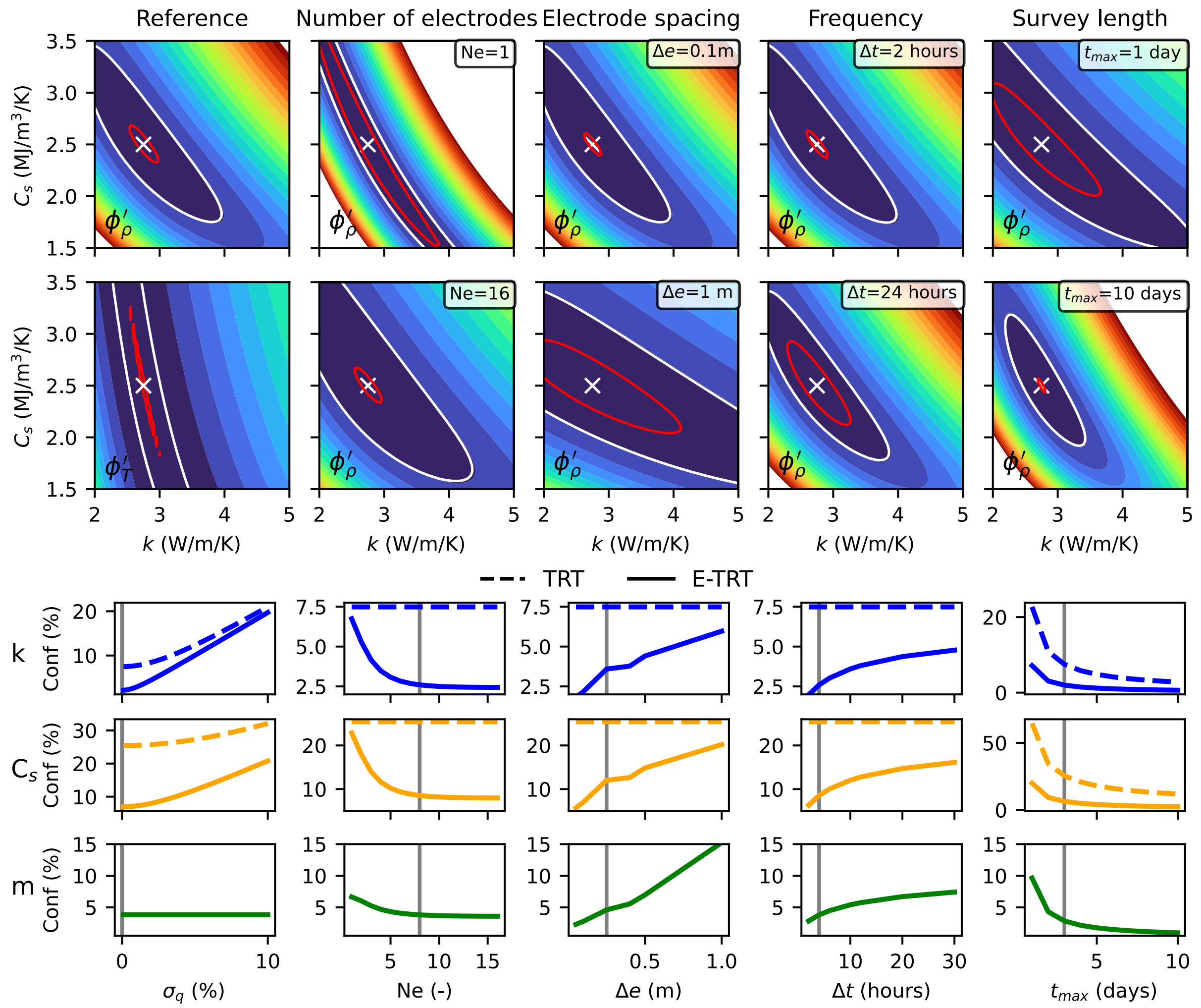

Fig. 12. Impact of E-TRT acquisition parameters. Top: Influence of acquisition settings on the shape of Φ'_ρ (Φ_ρ normalized by the number of ER data points) in the (k, C_s) parameter plane for m fixed at the solution. The white cross is the solution. The confidence region is plotted in red and the plotted white isocontour corresponds to $\Phi'_\rho = 1$. The first column displays Φ'_ρ (top) and Φ'_T (bottom) for the reference acquisition setup (see Table 1) Bottom: Effect of these acquisition parameters on the 95% confidence intervals for TRT and E-TRT datasets. The grey line is the reference case. (For interpretation of the references to colour in this figure legend, the reader is referred to the web version of this article.)

q is propagated to the MAP uncertainties. Fig. 12 (bottom-first column) illustrates how uncertainty of q increases uncertainty of k and C_s, while the impact on m remains minimal. These results show the importance of measuring q as precisely as possible for both TRT and E-TRT.

Appendix E. Effect of borehole water resistivity

Another critical factor for borehole ER measurements is the intrinsic electrical properties of the borehole water ρ_w and the rock ρ_r. Fig. 13 illustrates how water-to-rock resistivity ratio ρ_w/ρ_r influences the shape of Φ'_ρ in the (k, C_s) plane for the synthetic experiment. Table E.7 presents the MAP 95% confidence intervals for these ρ_w/ρ_r for $\rho_r = 10$ Ω m, using the errors described in Table 2. The corresponding ellipsoids are plotted in Fig. 13.

As ρ_w/ρ_r decreases, current channelling along the more conductive borehole water is favoured, and Φ'_ρ develops the shape of a valley, as ER measurements become increasingly sensitive to the borehole water rather than the bedrock formation. For the given reference acquisition, ER data provides a 61% improvement on the uncertainty of C_s for $\rho_w/\rho_r = 1$, 50 % when $\rho_w/\rho_r = 0.1$, still an improvement of 17% for ρ_w/ρ_r=0.01, but becomes ineffective (4% improvement) when $\rho_w/\rho_r = 0.001$. Comparatively, the impact on k and m is marginal with only a 4.1% and 2.9% difference, respectively, between $\rho_w/\rho_r = 1$ and $\rho_w/\rho_r = 0.001$. This is unsurprising for k, already well constrained by the TRT data, but more unexpected for m, indicating that its estimation requires only minimal sensitivity to the bedrock. To mitigate current channelling effects, previous studies have proposed placing electrodes on the surface of a PVC tube in the borehole (Tsourlos et al., 2003; LaBrecque et al., 1996) or using ring-shaped electrodes (Wagner et al., 2015). On the other hand, the bedrock resistivity does not alter the shape of Φ'_ρ near the solution, but it does affect the magnitude of $\Delta\rho_a$. Low bedrock resistivity yields smaller $\Delta\rho_a$ that are more sensitive to measurement noise. In contrast, geological formations with higher electrical resistivity will yield greater $\Delta\rho_a$ to temperature for the same

Table E.7
Effect of ρ_w/ρ_r on the MAP 95% confidence intervals for $\rho_r = 10$ Ωm. E-TRT values vary with ratio, while TRT values remain constant.

	ρ_w/ρ_r	k (%)	C_s (%)	m (%)
E-TRT	1	3.0	9.8	5.6
	0.1	3.8	12.8	5.5
	0.01	6.2	21.0	7.3
	0.001	7.1	24.3	8.5
TRT	all	7.5	25.4	–

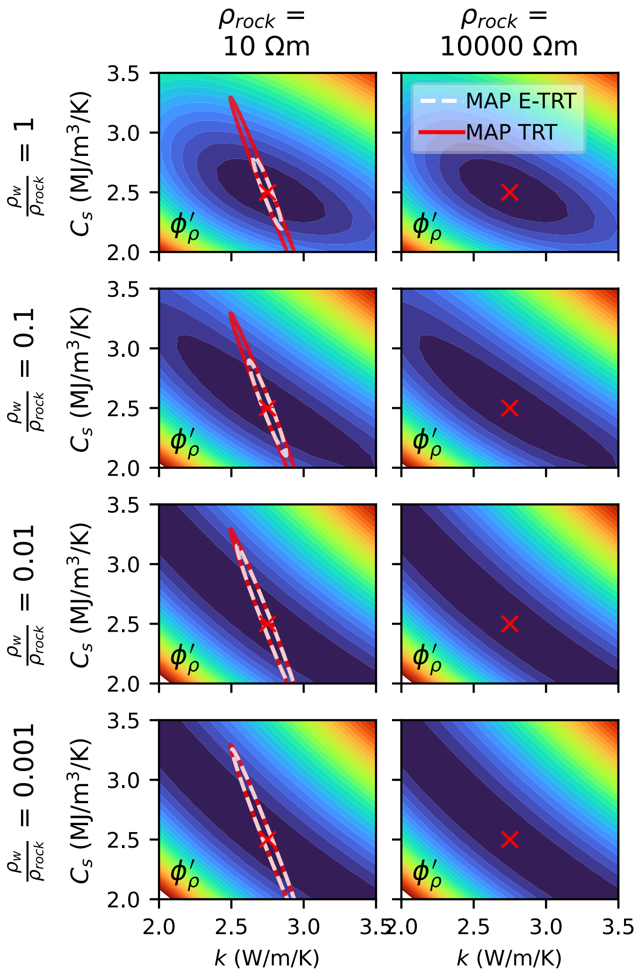

Fig. 13. Influence of rock electrical resistivity ρ_r and the resistivity ratio between water and rock resistivity ρ_w/ρ_r on the shape of Φ'_ρ for the k, C_s plane. The corresponding MAP ellipsoids are plotted for ρ_r = 10 Ω m.

relative change, enhancing signal-to-noise ratio for a fixed error. However, this benefit is tempered given that measurement error typically increases with resistivity (Tso et al., 2017), and that higher bedrock resistivity implies a lower ρ_w/ρ_r ratio, which may reduce sensitivity to the rock formation.

Data availability

All scripts and datasets used to generate the results and figures in this study are publicly available at: https://github.com/GeoCode-polymtl/E-TRT.

References

Arato, A., Boaga, J., Comina, C., De Seta, M., Di Sipio, E., Galgaro, A., Giordano, N., Mandrone, G., 2015. Geophysical monitoring for shallow geothermal applications – two Italian case histories. First Break 33 (8), http://dx.doi.org/10.3997/1365-2397.33.8.82010.

Archie, G.E., 1942. The electrical resistivity log as an aid in determining some reservoir characteristics. Trans. Soc. Pet. Eng. 146 (01), 54–62. http://dx.doi.org/10.2118/942054-G.

Aster, R.C., Borchers, B., Thurber, C.H., 2018. Parameter Estimation and Inverse Problems, third ed. Elsevier, http://dx.doi.org/10.1016/C2015-0-02458-3.

Beaudry, G., Pasquier, P., Marcotte, D., 2018. Hydrogeothermal characterization and modelling of a standing column well experimental installation. In: IGSHPA Research Track. http://dx.doi.org/10.22488/okstate.18.000009.

Binley, A., Slater, L., 2020. Resistivity and Induced Polarization: Theory and Applications to the Near-Surface Earth, first ed. Cambridge University Press, http://dx.doi.org/10.1017/9781108685955.

Carslaw, H.S., Jaeger, J.C., 1959. Conduction of Heat in Solids, second ed. Clarendon Press, Oxford.

Choi, W., Kikumoto, H., Choudhary, R., Ooka, R., 2018. Bayesian inference for thermal response test parameter estimation and uncertainty assessment. Appl. Energy 209, 306–321. http://dx.doi.org/10.1016/j.apenergy.2017.10.034.

Cockett, R., Kang, S., Heagy, L.J., Pidlisecky, A., Oldenburg, D.W., 2015. SimPEG: An open source framework for simulation and gradient based parameter estimation in geophysical applications. Comput. Geosci. http://dx.doi.org/10.1016/j.cageo.2015.09.015.

Comina, C., Giordano, N., Ghidone, G., Fischanger, F., 2019. Time-lapse 3D electric tomography for short-time monitoring of an experimental heat storage system. Geosciences 9 (4), 167. http://dx.doi.org/10.3390/geosciences9040167.

Dimech, A., Cheng, L., Chouteau, M., Chambers, J., Uhlemann, S., Wilkinson, P., Meldrum, P., Mary, B., Fabien-Ouellet, G., Isabelle, A., 2022. A review on applications of time-lapse electrical resistivity tomography over the last 30 years: Perspectives for mining waste monitoring. Surv. Geophys. 43, 1699–1759. http://dx.doi.org/10.1007/s10712-022-09731-2.

Doetsch, J.A., Coscia, I., Greenhalgh, S., Linde, N., Green, A., Günther, T., 2010. The borehole-fluid effect in electrical resistivity imaging. Geophysics 75 (4), F107–F114. http://dx.doi.org/10.1190/1.3467824.

Doll, H.G., 1953. Two decades of electrical logging. J. Pet. Technol. 5 (09), 33–41. http://dx.doi.org/10.2118/953091-G.

Florides, G.A., Kalogirou, S.A., 2008. First in situ determination of the thermal performance of a U-pipe borehole heat exchanger, in Cyprus. Appl. Therm. Eng. 28, 157–163. http://dx.doi.org/10.1016/j.applthermaleng.2007.03.026.

Fujii, H., Okubo, H., Nishi, K., Itoi, R., Ohyama, K., Shibata, K., 2009. An improved thermal response test for U-tube ground heat exchanger based on optical fiber thermometers. Geothermics 38 (4), 399–406. http://dx.doi.org/10.1016/j.geothermics.2009.06.002.

Gao, Q., Li, M., Yu, M., 2010. Experiment and simulation of temperature characteristics of intermittently-controlled ground heat exchanges. Renew. Energy 35 (6), 1169–1174. http://dx.doi.org/10.1016/j.renene.2009.10.039.

Gehlin, S., 2002. Thermal Response Test: Method Development and Evaluation (Ph.D. thesis). Luleå tekniska universitet.

Giordano, N., Arato, A., Comina, C., Mandrone, G., 2017. Time-lapse electrical resistivity imaging of the thermally affected zone of a borehole thermal energy storage system near torino (northern Italy). J. Appl. Geophys. 140, 123–134. http://dx.doi.org/10.1016/j.jappgeo.2017.03.015.

Goswami, J.C., Mydur, R., Wu, P., Heliot, D., 2004. A robust technique for well-log data inversion. IEEE Trans. Antennas Propagat. 52 (3), 717–724. http://dx.doi.org/10.1109/TAP.2004.825158.

Hayley, K., Bentley, L.R., Gharibi, M., Nightingale, M., 2007. Low temperature dependence of electrical resistivity : Implications for near surface geophysical monitoring. Geophys. Res. Lett. 34 (18), http://dx.doi.org/10.1029/2007GL031124.

Heagy, L.J., Cockett, R., Kang, S., Rosenkjaer, G.K., Oldenburg, D.W., 2017. A framework for simulation and inversion in electromagnetics. Computers Geosciences 107, 1–19. http://dx.doi.org/10.1016/j.cageo.2017.06.018.

Hermans, T., Vandenbohede, A., Lebbe, L., Nguyen, F., 2012. A shallow geothermal experiment in a sandy aquifer monitored using electric resistivity tomography. Geophysics 77, http://dx.doi.org/10.1190/geo2011-0199.1.

Hermans, T., Wildemeersch, S., Jamin, P., Orban, P., Brouyère, S., Dassargues, A., Nguyen, F., 2015. Quantitative temperature monitoring of a heat tracing experiment using cross-borehole ERT. Geothermics 53, 14–26. http://dx.doi.org/10.1016/j.geothermics.2014.03.013.

Huang, G., Liu, Y., Zhuang, C., Zhang, H., Lu, J., Zhu, L., 2020. Experimental study on heat transfer characteristics of helix ground heat exchanger coil under dynamic load. Therm. Sci. Eng. Prog. 18, 100546. http://dx.doi.org/10.1016/j.tsep.2020.100546.

Ingersoll, A.I., 1954. Heat Conduction with Engineering, Geological and Other Applications. University of Wisconsin Press.

Itskovich, G., Mezzatesta, A., Strack, K.-M., Tabarovsky, L., 1998. High-definition lateral log resistivity device: basic physics and resolution. In: Trans SPWLA 39th Annual Logging Symposium. Houston, Texas, Paper V.

Jacques, L., Pasquier, P., 2023. Obtaining the hydraulic and thermal properties of the main hydrostratigraphic units surrounding a standing column well using a thermal response test. J. Hydrol. 623, http://dx.doi.org/10.1016/j.jhydrol.2023.129823.

Jacques, L., Pasquier, P., Dion, G., Beaudry, G., 2025. Experimental assessment of interwell reinjection in standing column wells by analysis of transfer functions obtained from non-stationary deconvolution. Geothermics 125, 103184. http://dx.doi.org/10.1016/j.geothermics.2024.103184.

Jalaluddin, Miyara, A., 2012. Thermal performance investigation of several types of vertical ground heat exchangers with different operation mode. Appl. Therm. Eng. 33–34, 167–174. http://dx.doi.org/10.1016/j.applthermaleng.2011.09.030.

Koohi-Fayegh, S., Rosen, M.A., 2018. Long-term study of vertical ground heat exchangers with varying seasonal heat fluxes. Geothermics 75, 15–25. http://dx.doi.org/10.1016/j.geothermics.2018.03.010.

Kristinsdóttir, L.H., Flóvenz, Ó.G., Árnason, K., Bruhn, D., Milsch, H., Spangenberg, E., Kulenkampff, J., 2010. Electrical conductivity and P-wave velocity in rock samples from high-temperature icelandic geothermal fields. Geothermics 39, 94–105. http://dx.doi.org/10.1016/j.geothermics.2009.12.001.

Kyrkou, K., Booth, A., Ngui, Y.J., Chambers, J., Loveridge, F., Kelly, J., Smith, E., Nowacki, A., Hough, E., Boon, D., Kuras, O., 2024. Geophysical surveys to inform heat-flow experiments in a fractured chalk aquifer, berkshire, UK. In: EGU General Assembly 2024. Vienna, Austria, pp. EGU24–12616. http://dx.doi.org/10.5194/egusphere-egu24-12616.

LaBrecque, D.J., Ramirez, A.L., Daily, W.D., Binley, A.M., Schima, S.A., 1996. ERT monitoring of environmental remediation processes. Meas. Sci. Technol. 7 (3), 375. http://dx.doi.org/10.1088/0957-0233/7/3/019.

Lesparre, N., Robert, T., Nguyen, F., Boyle, A., Hermans, T., 2019. 4D electrical resistivity tomography (ERT) for aquifer thermal energy storage monitoring. Geothermics 77, 368–382. http://dx.doi.org/10.3390/en7085083.

Li, M., Lai, A.C.K., 2012. Parameter estimation of in-situ thermal response tests for borehole ground heat exchangers. Int. J. Heat Mass Transfer 55 (9–10), 2615–2624. http://dx.doi.org/10.1016/j.ijheatmasstransfer.2011.12.033.

Li, M., Zhang, L., Liu, G., 2019. Estimation of thermal properties of soil and backfilling material from thermal response tests (TRTs) for exploiting shallow geothermal energy: Sensitivity, identifiability, and uncertainty. Renew. Energy 132, 1263–1270. http://dx.doi.org/10.1016/j.renene.2018.09.022.

Loke, M.H., 2001. Electrical imaging surveys for environmental and engineering studies. A practical guide to 2-D and 3-D surveys.

Lund, J.W., Toth, A.N., 2021. Direct utilization of geothermal energy 2020 worldwide review. Geothermics 90, 101915. http://dx.doi.org/10.1016/j.geothermics.2020.101915.

Ma, R., McBratney, A., Whelan, B., Minasny, B., Short, M., 2011. Comparing temperature correction models for soil electrical conductivity measurement. Precis. Agric. 12 (1), 55–66. http://dx.doi.org/10.1007/s11119-009-9156-7.

Márquez, J.M.A., Bohórquez, M.Á.M., Melgar, S.G., 2016. Ground thermal diffusivity calculation by direct soil temperature measurement. Application to very low enthalpy geothermal energy systems. Sensors 16 (3), 306. http://dx.doi.org/10.3390/s16030306.

McDaniel, A., Tinjum, J., Hart, D.J., Lin, Y.-F., Stumpf, A., Thomas, L., 2018. Distributed thermal response test to analyze thermal properties in heterogeneous lithology. Geothermics 76, 116–124. http://dx.doi.org/10.1016/j.geothermics.2018.07.003.

Nimmer, R.E., Osiensky, J.L., Binley, A.M., Williams, B.C., 2008. Three-dimensional effects causing artifacts in two-dimensional, cross-borehole, electrical imaging. J. Hydrol. 359 (1–2), 59–70. http://dx.doi.org/10.1016/j.jhydrol.2008.06.022.

Nono, F., Gibert, B., Parat, F., Loggia, D., Cichy, S., et al., 2020. Electrical conductivity of icelandic deep geothermal reservoirs up to supercritical conditions: Insight from laboratory experiments. J. Volcanol. Geotherm. Res. 391, 106364. http://dx.doi.org/10.1016/j.jvolgeores.2018.04.021.

Özüdoğru, A., Olgun, G.C., Senol, T.Y., 2014. 3D numerical modeling of vertical geothermal heat exchangers. Geothermics 51, 312–324. http://dx.doi.org/10.1016/j.geothermics.2014.02.005.

Pasquier, P., 2015. Stochastic interpretation of thermal response test with TRT-SInterp. Comput. Geosci. 75, 73–87. http://dx.doi.org/10.1016/j.cageo.2014.11.001.

Pasquier, P., Marcotte, D., 2020. Robust identification of volumetric heat capacity and analysis of thermal response tests by Bayesian inference with correlated residuals. Appl. Energy 261, 114394. http://dx.doi.org/10.1016/j.apenergy.2019.114394.

Pasquier, P., Zarrella, A., Marcotte, D., 2019. A multi-objective optimization strategy to reduce correlation and uncertainty for thermal response test analysis. Geothermics 79, 176–187. http://dx.doi.org/10.1016/j.geothermics.2019.02.003.

Raymond, J., Therrien, R., Gosselin, L., Lefebvre, R., 2011. A review of thermal response test analysis using pumping test concepts. Ground Water 49 (6), 932–945. http://dx.doi.org/10.1111/j.1745-6584.2010.00791.x.

Rees, S.J., Spitler, J.D., Deng, Z., Orio, C.D., Johnson, C.N., 2004. A Study of Geothermal Heat Pump and Standing Column Well Performance. ASHRAE Transactions.

Revil, A., Cathles, L., Losh, S., Nunn, J., 1998. Electrical conductivity in shaly sands with geophysical applications. J. Geophys. Res.: Solid Earth 103 (B10), 23925–23936. http://dx.doi.org/10.1029/98JB02125.

Robert, T., Hermans, T., Dumont, G., Nguyen, F., Rwabuhungu, D.E., 2013. Near surface geoscience. In: Reliability of ERT-Derived Temperature—Insights from Laboratory Measurements. http://dx.doi.org/10.3997/2214-4609.20131373.

Robert, S., Pasquier, P., Nguyen, A., 2022. Impact of layered heterogeneity on thermal response test interpretation performed on a standing column well operated without bleed. Geothermics 101, 102353. http://dx.doi.org/10.1016/j.geothermics.2022.102353.

Shariatinik, B., Gloaguen, E., Raymond, J., Boutin, L.C., Fabien-Ouellet, G., 2024. ERT data assimilation to characterize aquifer hydraulic conductivity heterogeneity through a heat-tracing experiment. Near Surface Geophy. 22 (3), 358–371. http://dx.doi.org/10.1002/nsg.12288.

Signorelli, S., Bassetti, S., Pahud, D., Kohl, T., 2007. Numerical evaluation of thermal response tests. Geothermics 36 (2), 141–166. http://dx.doi.org/10.1016/j.geothermics.2006.10.006.

Spitler, J.D., Gehlin, S.E.A., 2015. Thermal response testing for ground source heat pump systems—An historical review. Renew. Sustain. Energy Rev. 50, 1125–1137. http://dx.doi.org/10.1016/j.rser.2015.05.061.

Spitler, J.D., Rees, S.J., Deng, Z., Chiasson, A., Orio, C.D., Johnson, C., 2002. R&D Studies Applied to Standing Column Well Design. Final Report ASHRAE 1119-RP, Oklahoma State University, School of Mechanical and Aerospace Engineering, Water and Energy Systems Corporation.

Sundberg, J., 1988. Thermal properties of soils and rocks. Thése, Statens geotekniska institut, Linköping.

Tarantola, A., 2005. Inverse Problem Theory and Methods for Model Parameter Estimation. Society for Industrial and Applied Mathematics, http://dx.doi.org/10.1137/1.9780898717921.

Tso, C.-H.M., Kuras, O., Wilkinson, P.B., Uhlemann, S., Chambers, J.E., Meldrum, P.I., Graham, J., Sherlock, E.F., Binley, A., 2017. Improved characterisation and modelling of measurement errors in electrical resistivity tomography (ERT) surveys. J. Appl. Geophys. 138, 103–119. http://dx.doi.org/10.1016/j.jappgeo.2017.09.009.

Tsourlos, P., Ogilvy, R., Meldrum, P., Williams, G., 2003. Time-lapse monitoring in single boreholes using electrical resistivity tomography. J. Environ. Eng. Geophys. 8 (1), 1–14. http://dx.doi.org/10.4133/JEEG8.1.1.

Ulugergerli, E.U., 2011. Two dimensional combined inversion of short- and long-normal dc resistivity well log data. J. Appl. Geophys. 73 (2), 130–138. http://dx.doi.org/10.1016/j.jappgeo.2010.12.004.

Wagner, F.M., Bergmann, P., Rücker, C., Maurer, H., et al., 2015. Impact and mitigation of borehole related effects in permanent crosshole resistivity imaging: An example from the Ketzin CO2 storage site. J. Appl. Geophys. 123, 102–111. http://dx.doi.org/10.1016/j.jappgeo.2015.10.005.

Wagner, R., Clauser, C., 2005. Evaluating thermal response tests using parameter estimation for thermal conductivity and thermal capacity. J. Geophys. Eng. 2 (4), 349–356. http://dx.doi.org/10.1088/1742-2132/2/4/S08.

Waxman, M., Smits, L., 1968. Electrical conductivities in oil-bearing shaly sands. SPE J. 8 (2), 107–122. http://dx.doi.org/10.2118/1863-A.

Yuill, G.K., Mikler, V., 1995. Analysis of the effect of induced groundwater flow on heat transfer from a vertical open-hole concentric-tube thermal well. ASHRAE Trans. 101, 173–185.

Zhang, C., Song, W., Sun, S., Peng, D., 2015. Parameter estimation of in-situ thermal response test with unstable heat rate. Energy 88, 497–505. http://dx.doi.org/10.1016/j.energy.2015.05.074.